Bioactive Materials 33 (2024) 572–590

Contents lists available at ScienceDirect

Bioactive Materials

journal homepage: www.keaipublishing.com/en/journals/bioactive-materials

Skin derived precursors induced Schwann cells mediated tissue engineering-aided neuroregeneration across sciatic nerve defect

Chengbin Xue [a,*,1], Hui Zhu [a,1], Hongkui Wang [a,1], Yaxian Wang [a,1], Xi Xu [a,b,1], Songlin Zhou [a], Dong Liu [a], Yahong Zhao [a], Tianmei Qian [a], Qi Guo [a,c], Jin He [d], Kairong Zhang [d], Yun Gu [a], Leilei Gong [a], Jian Yang [a], Sheng Yi [a], Bin Yu [a], Yongjun Wang [a], Yan Liu [a], Yumin Yang [a], Fei Ding [a], Xiaosong Gu [a,**]

[a] Jiangsu Clinical Medicine Center of Tissue Engineering and Nerve Injury Repair, Research Center of Clinical Medicine, Affiliated Hospital of Nantong University, Key Laboratory of Neuroregeneration of Jiangsu and Ministry of Education, Co-innovation Center of Neuroregeneration, Nantong University, Nantong, JS, 226001, PR China
[b] Department of Rehabilitation Medicine, Affiliated Hospital of Nantong University, Nantong, JS, 226001, PR China
[c] Department of Hand Surgery, China-Japan Union Hospital, Jilin University, Changchun, PR China
[d] Medical School of Nantong University, Nantong, JS, 226001, PR China

ARTICLE INFO

Keywords:
SKP-SCs-TEN
Transcriptomic feature
Reconstruction of regenerative microenvironment
Molecular regulation
Molecular regenerative-medicine

ABSTRACT

A central question in neural tissue engineering is how the tissue-engineered nerve (TEN) translates detailed transcriptional signals associated with peripheral nerve regeneration into meaningful biological processes. Here, we report a skin-derived precursor-induced Schwann cell (SKP-SC)-mediated chitosan/silk fibroin-fabricated tissue-engineered nerve graft (SKP–SCs-TEN) that can promote sciatic nerve regeneration and functional restoration nearly to the levels achieved by autologous nerve grafts according to behavioral, histological, and electrophysiological evidence. For achieving better effect of neuroregeneration, this is the first time to jointly apply a dynamic perfusion bioreactor and the ascorbic acid to stimulate the SKP-SCs secretion of extracellular matrix (ECM). To overcome the limitation of traditional tissue-engineered nerve grafts, jointly utilizing SKP-SCs and their ECM components were motivated by the thought of prolongating the effect of support cells and their bioactive cues that promote peripheral nerve regeneration. To further explore the regulatory model of gene expression and the related molecular mechanisms involved in tissue engineering-aided peripheral nerve regeneration, we performed a cDNA microarray analysis of gene expression profiling, a comprehensive bioinformatics analysis and a validation study on the grafted segments and dorsal root ganglia tissues. A wealth of transcriptomic and bioinformatics data has revealed complex molecular networks and orchestrated functional regulation that may be responsible for the effects of SKP-SCs-TEN on promoting peripheral nerve regeneration. Our work provides new insights into transcriptomic features and patterns of molecular regulation in nerve functional recovery aided by SKP-SCs-TEN that sheds light on the broader possibilities for novel repair strategies of peripheral nerve injury.

1. Introduction

Although peripheral nerves have some regenerative capacity after traumatic injury, their regeneration rate is slow, and functional recovery is poor without clinical intervention, especially in cases with substantial nerve defects. Autologous nerve grafting, i.e., implantation of autologous nerve grafts into the defect has been accepted as the standard-of-care for surgical repair of peripheral nerve injury (PNI) [1]. As a potential substitute for autologous nerve grafts for peripheral nerve regeneration, the emergence and development of neural tissue engineering, including the creation of tissue-engineered nerves (TENs), has been stimulated by the inherent limitations of the gold-standard [2].

Peer review under responsibility of KeAi Communications Co., Ltd.
* Corresponding author.
** Corresponding author.
E-mail addresses: xue_chengbin@hotmail.com (C. Xue), nervegu@ntu.edu.cn (X. Gu).
[1] Contributed equally to this work.

https://doi.org/10.1016/j.bioactmat.2023.11.016
Received 21 July 2023; Received in revised form 8 November 2023; Accepted 23 November 2023

TEN usually consists of a biomaterial-constructed neural scaffold, physical cues (such as electrical stimulation), and biological cues (such as support cells and/or growth factors) to meet the requirements of building a favorable regenerative microenvironment and enhancing the intrinsic ability of axonal regrowth [3,4]. To date, many TENs with different compositions and configurations have been constructed for bridging peripheral nerve defects in a diverse array of animal models ranging from rodents to nonhuman primates. Most TEN designs achieve the desired outcomes of neural regeneration and functional repair [2], and some are now FDA-approved commercial products that are available for use in preclinical and clinical trials [5–7].

Following PNI, especially for peripheral nerve defects, the axons degenerate and regenerate. The injured axons must regenerate back to their target muscles and then recover their functions [8]. Thus, the axons must navigate through microenvironments and are noted as the bridge of nerve defects by new tissue, including the distal nerve stump [9]. This regeneration involves a series of complicated multicellular processes, including morphological degeneration of nerve tissue, cellular phenotypic and functional alterations, and a myriad of genomic and transcriptomic changes. Moreover, increasing attention has been focused on discovering transcriptomic features induced by PNI. It is also hypothesized that some transcriptional regulators may support injured neuron survival and axon regeneration *in vivo* [10]. To understand the molecular mechanisms underlying PNI and regeneration, we used a high-throughput microarray platform in combination with bioinformatics analysis to investigate molecular regulation during the post-injury process. The important findings of previous studies have contributed to the development of more effective therapeutic strategies for peripheral nerve repair, though they have focused on PNI not treated with any other therapeutic measures [11–13]. In contrast, the molecular properties underlying peripheral nerve repair that are aided by nerve grafting, especially with TEN, have not yet been fully elucidated.

We hypothesized that the TEN also better promotes sciatic nerve regeneration. To test this hypothesis, the TENs we used were prepared by introducing SKP-Schwann cells (SCs) into a chitosan/silk fibroin-fabricated neural scaffold. SKPs are commonly known as a novel population of neural crest precursor cells within the dermis [14,15] and can be obtained from adult skin [16]. SKPs contribute to the growth of hair follicles, sustain the dermis, and aid in repair following injury [15]. Both rodent and human SKPs can differentiate into skin-derived precursor--induced Schwann cells (SKP–SCs) that express markers of SCs, including S100β, glial fibrillary acidic protein (GFAP), and p75 neurotrophin receptor ($P75^{NTR}$), and myelinate axons *in vitro* or *in vivo* [17–19]. Therefore, these cells were selected as support cells for inclusion in the TENs. As for the scaffold material, both chitosan and silk fibroin are naturally derived biomaterials with suitable biocompatibility, biodegradability, and neuro-affinity that are beneficial for peripheral nerve regeneration [20,21]. We used a chitosan-based nerve conduit and luminal fillers of silk fibroin fibers to construct neural scaffolds for the TEN.

To further investigate the transcriptomic features of lesioned peripheral nerves after receiving the following treatments: implantation of SKP-SC-TEN, autologous nerve grafts, or chitosan/silk fibroin-fabricated neural scaffolds, we used the SKP-SC-containing, chitosan/silk fibroin-fabricated TEN to bridge a 10-mm sciatic nerve defect in rats and assessed the repair outcomes by conducting behavioral, functional, and morphological evaluations at three months post-nerve injury. After observing the beneficial effects of the TEN on peripheral nerve repair, we collected total RNA samples from the regenerated segment of the sciatic nerve and the corresponding dorsal root ganglia (DRGs) of animals that had undergone treatment with TEN, autologous nerve grafts, or chitosan/silk fibroin-fabricated neural scaffolds at a series of post-operative time points for microarray analysis. The resulting global transcriptomic profiles, highlighted several biological processes occurring in the sciatic nerve grafts and the corresponding DRGs during nerve repair including cell apoptosis, axonal regeneration, remyelination, revascularization, and their transcriptional regulation (Graphic Abstract). Our data collectively contributes to the understanding of the transcriptomic features involved in peripheral nerve repair with TEN.

2. Results

2.1. Characterizations of SKPs and SKP-SCs

To isolate and purify SKPs from the skin of wild type (WT) newborn rats, an optimized protocol was carried out as described previously [22] with minor modifications. Skin tissue collected from the backs of newborn rats were sectioned and followed by hematoxylin and eosin (H&E) staining. The location of SKPs was determined by immunostaining with SKP markers nestin, vimentin, versican, and fibronectin. SKP spheres were generated from juvenile SKPs after 14 days of culture (Fig. 1a). To characterize the harvested SKPs, double-immunostaining for nestin, sca-1, versican, fibronectin, or vimentin with Hoechst 33342 was performed (Fig. 1b). Then, SKPs were successfully differentiated into SKP-SCs *in vitro*, as evidenced by labeling with SC markers, such as S100β, GFAP and $p75^{NTR}$ (Fig. 1c) [17,22].

To investigate the function of SKP-SCs *in vitro* and to trace the fate of SKP-SCs *in vivo*, green fluorescent protein (GFP)-labeled SKPs (Fig. S1a) isolated from the back skin of GFP-transgenic newborn rats were differentiated to yield GFP-SKP-SCs, which were further used in the construction of TENs (Fig. S1b). GFP-SKP-SCs were cocultured with DRG-derived axons for one week. SKP-SCs were observed by a scanning electron microscope (SEM) (Figs. S1c–d). SKP-SCs aligned along and wrapped around axons (Figs. S1e–f). After more than two weeks of coculture, a portion of SKP-SCs began to sheath DRG axons and formed myelin-like structures (Figs. S1g–h). Triple-immunostaining with MBP, P0, or MAG (myelin markers), NF-200 (axon marker), and Hoechst 33342 (cell nucleus marker) provided further evidence of functional characterization of the SKP-SCs that we obtained (Figs. S1i–k). These results demonstrated the myelinating ability of SKP-SCs, in accordance with previous work published by other groups [17].

2.2. Fabrication of TEN and tracing of GFP-SKP-SCs in vivo

To fabricate the standardized TEN efficiently, we prepared a chitosan/silk fibroin neural scaffold with a perfusion bioreactor (termed the RCCMax system) [23], which continuously provided oxygen and nutrition while removing metabolites (Fig. 1d and Movie S1). After GFP-SKP-SCs attached to the surface of the neural scaffold, ascorbic acid was added to stimulate the secretion of extracellular matrix (ECM) within one week, which provided a permissive surface and microenvironment to support axonal regeneration [20,21,24]. To characterize cellular components of the fabricated TEN, SEM was used to show the micromorphology of SKP-SCs (Fig. 1e). The cell phenotype was further confirmed by immunostaining with SC markers (S100β, GFAP and $p75^{NTR}$), while immunostaining with ECM molecules (collagen I, collagen IV, fibronectin and laminin) confirmed that ECM molecules were also contained in the TEN (Fig. 1f).

We then sought to determine the role of SKP-SCs during neuroregeneration. The GFP-SKP-SCs were cultured on a silk fibroin filament-chitosan conduit (Fig. 1e). At three weeks post-implantation of the TEN, a linear end-to-end arrangement of GFP-SKP-SCs was observed at the implantation site, suggesting that SKP-SCs contained in the TEN could survive at least three weeks after implantation (Fig. 1g).

2.3. Repair of peripheral nerve defect by TEN

To evaluate the recovery of locomotor function in rats treated with different methods, the CatWalk™ gait analysis system was utilized to calculate the sciatic function index (SFI) to monitor recovery [21]. Better metatarsophalangeal joint plantar flexion and toe spreading were observed in the animals treated with TENs and autografts compared to

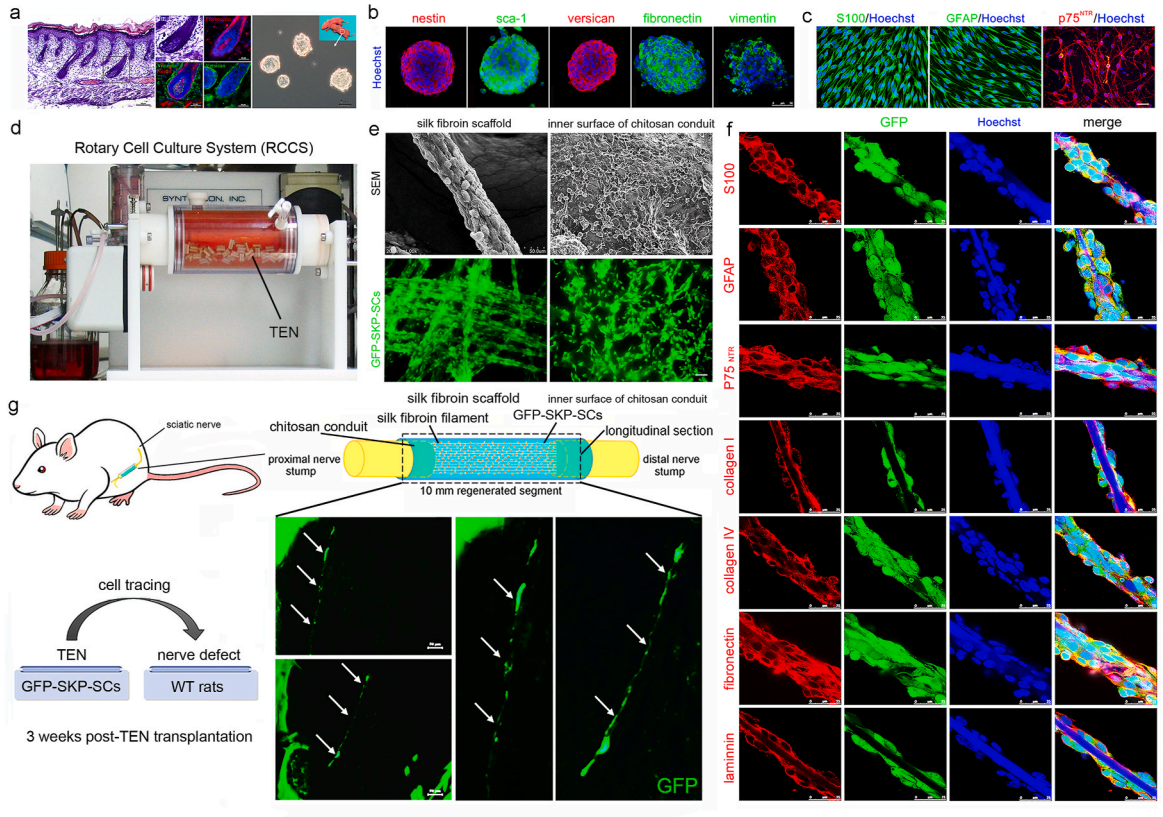

Fig. 1. | Construction of TEN *in vitro* and tracing of GFP-SKP-SCs *in vivo*. (a) Isolation and culture of SKPs from the back skin of 1 to 3-day-old newborn rat. HE staining and immunostainings of fibronectin, nestin, vimentin, and versican showed the location of SKPs around the dermal hair follicle area of the newborn rat. Phase contrast image showed the SKP spheres were generated from juvenile SKPs after 14 days of culture. (b) Characterizations by the immunostainings of nestin, sca-1, vimentin, fibronectin, and versican for SKPs and (c) the immunostainings of S100β, GFAP and p75 ^{NTR} for SKP-SCs. (d) The GFP-SKP-SCs cultured with chitosan/silk fibroin neural scaffolds in a perfusion bioreactor (termed the RCCMax system). (e) SEM images and immunofluorescence images showed the micromorphology of GFP-SKP-SCs cultured on silk fibroin filaments and chitosan conduit. (f) SCs markers (S100 β, GFAP and p75 ^{NTR}) and ECM molecules (collagen I, collagen IV, fibronectin and laminin) were confirmed by immunostainings on the silk fibroin filaments 7 days post construction of TEN. (g) The GFP-SKP-SCs-containing, chitosan/SF-fabricated TEN was applied in repairing the 10 mm sciatic nerve defect in wild type rat. The grafting segment was obtained, sectioned longitudinally, and then subjected to GFP fluorescent monitoring under microscopic observation. A linear end-to-end arrangement of GFP-SKP-SCs was observed at the implantation site three weeks post-implantation of the TEN.

those treated with only the scaffold (Fig. 2a, Movie S2-4). At 8- or 12-weeks post-surgery, SFI values of both TEN and autograft groups were significantly better than that of the scaffold group (Fig. 2b). As expected, SFI values of the nongrafted group were consistently near −100 (complete dysfunction) at all time points post-surgery.

To further evaluate to functional recovery, the amplitude of compound muscle action potential (CMAP) recordings and the motor conduction velocity (MCV) calculations were performed in animals among different groups at 12 weeks post-surgery (Fig. 2c). CMAP and MCV usually show positive correlations with the number of nerve fibers innervating the muscle and the myelin sheath thickness or the diameter of myelinated nerve fibers, respectively [25]. MCV recovery ratio and CMAP amplitude in both TEN and autograft groups were superior than those in the scaffold group, and no significant difference was observed in either CMAP or MCV between the TEN and autograft groups (Fig. 2d). However, both CMAP and MCV recovery ratios were around 60 % in the TEN and autograft groups, suggesting an elongated period is required to obtain full restoration to the normal level [26].

Next, to assess the reconstruction of the neural pathway and axonal transportation *in vivo*, Fluoro-Gold (FG)-labeled motor and sensory neurons were traced on both the ipsilateral (injured) side and contralateral (uninjured) side of spinal cord (anterior horn) and DRG tissues, respectively (Fig. 2e). The FG particles were found spreading in the cell body and axons of neurons. No obvious difference was observed between the TEN and autograft groups either in the total number or the percentage of FG-labeled motor neurons and sensory neurons. Notably, significantly more neurons in the TEN and autograft groups were labeled with FG than those in the scaffold group, suggesting a superior reconstruction of neural pathway and axonal transportation in the former groups.

The wet weight ratio and morphology of the gastrocnemius and anterior tibial muscle were analyzed to determine the degree of target muscle atrophy and reinnervation of the regenerated sciatic nerve. The frozen cross-sections were obtained from the mid-belly of gastrocnemius muscles and were stained with Masson's trichrome. The results indicated a better recovery in the size of muscle fibers in both TEN and autograft groups than in the scaffold group. In the nongrafted group, the muscle fibers showed severe atrophy and sections were rich in connective tissues (collagen stained blue) (Fig. 2f). Morphometric analysis showed insignificant differences in the wet weight ratio and the average cross-sectional area of muscle fibers in the TEN and autograft groups, however these groups were still superior to animals treated with the scaffold alone. Unsurprisingly, the untreated group averaged the worst muscle fiber cross-sectional area of all the trial groups (Fig. 2f). To further investigate the formation of motor endplates in target muscles, double staining of α-bungarotoxin and NF-200 antibody were performed (Fig. 2g). The level of reinnervation in target muscles of the sciatic nerve in TEN and autograft groups was superior to that in scaffold group. These discoveries are identical with the results of our electrophysiological evaluation, jointly demonstrating that the TEN better prevents

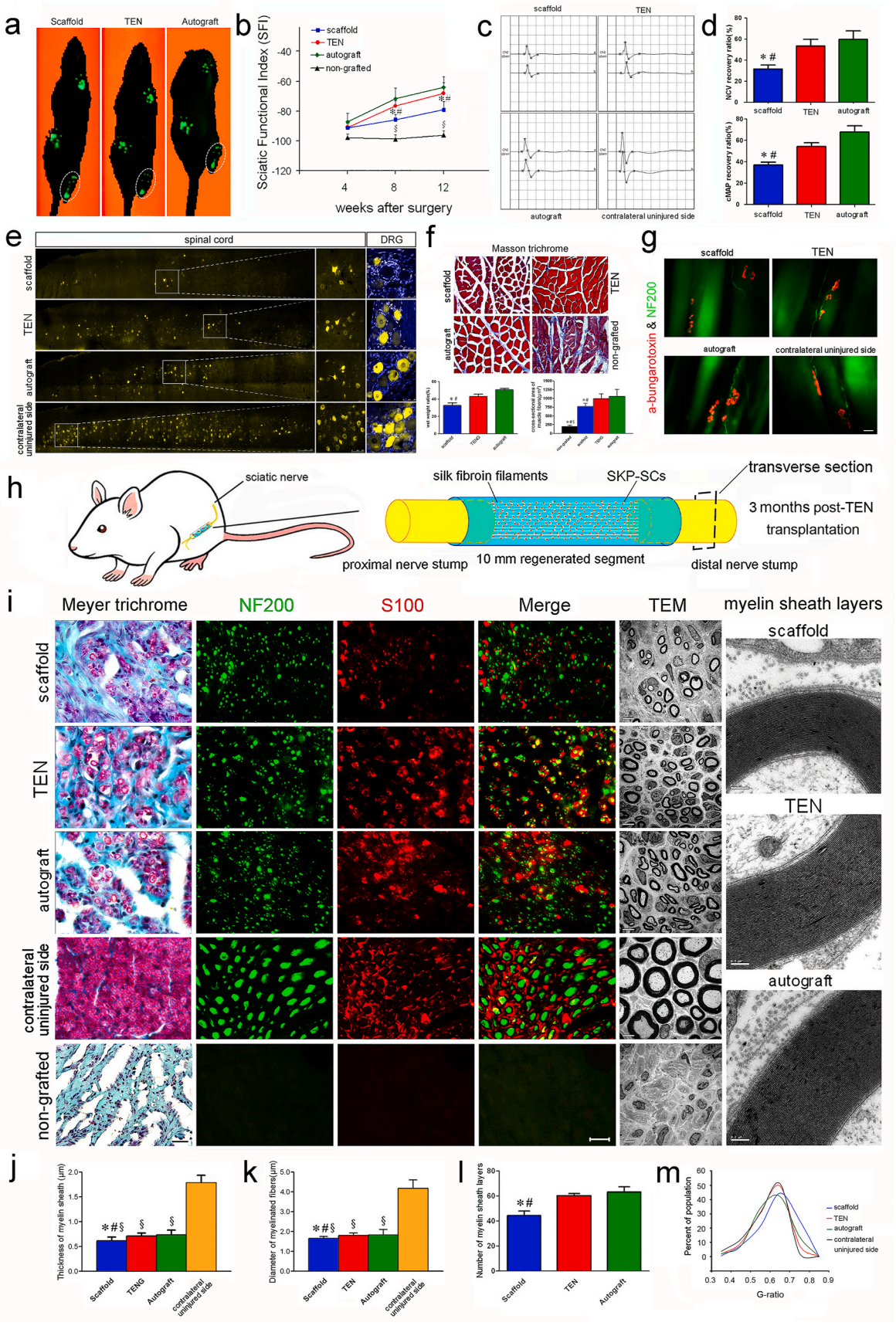

(caption on next page)

Fig. 2. | Repair of sciatic nerve defect in rat by TEN. (a) At 4 w, 8 w, 12 w post-surgery, CatWalk™ gait analysis system was applied to obtain the sciatic function index (SFI) of animals which were bridged with TENs, autologous nerve grafts and chitosan/fibroin scaffolds, respectively. Representative footprints at 12 w post-surgery were indicated by dotted ellipse. (b) Histogram comparing the SFI values among three groups at different time points post-surgery. $^{*}p < 0.05$ versus TEN group, $^{\#}p < 0.05$ versus autograft group and $^{\S}p < 0.05$ versus scaffold group. (c) Representative CMAP recordings at 12 weeks post-surgery, were obtained from the injured side of animals in scaffold, TEN, autograft groups and on the contralateral uninjured side of animals, respectively. (d) Histograms showing the recovery ratios of the motor nerve conduction velocity and CMAP amplitude detected on the injured side of animals in the scaffold, TEN and autograft groups, respectively. $^{*}p < 0.05$ versus TEN group, and $^{\#}p < 0.05$ versus autograft group. (e) Representative fluorescence micrographs following FluoroGold™ (FG) retrograde nerve tracing. FG retrogradely labeled motor neurons in the spinal cord and sensory neurons in DRGs (double-labeled with Hoechst 33342 (blue) for clearly showing outlines of the sensory neurons). The high magnifications of the boxed areas clearly showed the FG-labeled motor neurons in longitudinal sections of spinal cord, respectively. Scale bar: 250 μm for low magnifications of spinal cord, 100 μm for high magnifications of spinal cord and 50 μm for DRGs. (f) Masson's trichrome staining obtained at 12 weeks post-surgery, of the sectioned gastrocnemius muscle. Scale bar, 20 mm. Histograms showing the wet weight ratio of total anterior tibialis and gastrocnemius muscle, and the cross-sectional area of gastrocnemius muscle fibers. Data are expressed as means ± SD. $^{*}p < 0.05$ versus TEN group, $^{\#}p < 0.05$ versus autograft group and $^{\S}p < 0.05$ versus the scaffold group. (g) Photomicrographs of longitudinal sections of gastrocnemius muscles at the injured side after α-bungarotoxin staining of motor endplates (red) and immunohistochemistry with anti-NF200 (green) of regenerated axons were applied to animals in three groups at 12 weeks after nerve grafting and the contralateral uninjured side muscle. Scale bar: 20 μm. (h) Illustration of histological observation and morphometric analysis of the regenerated nerve at 12 weeks post-surgery. (i) Meyer trichrome staining, double immunostaining with anti-NF200 (green) and anti-S100 (red), and transmission electron micrographs (high magnifications for myelin lamellae), obtained at 12 weeks post-surgery. Scale bar: 10 μm for Meyer trichrome staining sections, 20 μm for immunostaining photomicrographs, 5 μm for TEM images and 0.2 mm for myelin lamellae images. Histograms showing the thickness of the regenerated myelin sheath (j), the diameter of regenerated myelinated nerve fibers (k), and the number of regenerated myelin lamella (l). Data are expressed as means ± SD. One-way ANOVA and the post hoc Bonferroni *t*-test were used to analyze the data. $^{*}p < 0.05$ versus TEN group, $^{\#}p < 0.05$ versus autograft group and $^{\S}p < 0.05$ versus the contralateral uninjured side of animals. (m) To analysis of myelinated nerve fibers in regenerated nerves, normalized frequency distributions of G-ratios (axon/fiber diameter) in scaffold, TEN, autograft groups and the contralateral uninjured side of animals, respectively. The distribution of regenerated nerves in TEN group and the contralateral uninjured side were similar and significantly different from that of the scaffold and autograft groups ($p < 0.05$, KolmogorovSmirnov test). Nine animals per group were used for measurements.

muscle atrophy and improves the subsequent reinnervation of the target muscles.

To obtain the histological evaluation of regenerated nerves harvested at 12 weeks post-surgery, the transverse sections of the distal nerve stump (Fig. 2h) stained by Meyer's trichrome, NF200 and S100 antibodies indicated that there were massive bundles of myelinated nerve fibers dispersed in clusters in both the TEN and autograft groups. These were demonstrated by transmission electron microscopy (TEM) that the myelinated axons were surrounded by electron-dense myelin sheaths, also shown in the lamellae structure of regenerated myelin sheaths. In contrast, disoriented distribution of cells in degenerated fascicules and obvious hyperplasia of connective tissues without regenerated nerve fibers were observed in the nongrafted group (Fig. 2i).

As one of the most important aspects of measuring peripheral nerve repair, the regenerated myelinated nerve fibers are frequently assessed by means of various parameters such as the thickness of the myelin sheath, the diameter of myelinated fibers, and the number of regenerated myelin lamellae. Statistical results of the thickness of the myelin sheath (Fig. 2j), the diameter of myelinated fibers (Fig. 2k), and the number of regenerated myelin lamellae (Fig. 2l) showed insignificant differences between the TEN and autograft groups, and superiority relative to the scaffold group. These parameters on the injured side had not completely reached the level of those on the contralateral side. The G-ratio, an index for evaluating the distribution of myelinated nerve fibers, between the ipsilateral and contralateral sides in the TEN group were similar (Fig. 2m). This was unique to the TEN and was significantly different compared to the same metric in the scaffold and autograft groups. All of the results indicate improved reconstruction of the rat sciatic nerve function at 12 weeks following implantation of the TEN.

2.4. Overview of transcriptomic features in regenerative nerve segments and the corresponding DRG tissues following sciatic nerve injury

To investigate the transcriptional events in injured neurons, we investigated the transcriptional mechanisms that regulate a wide variety of regeneration-associated genes to coordinate functional regeneration. We performed comprehensive and integrated transcriptomic analysis to delineate gene regulatory programs that drive the regenerative trajectory both in the regenerative nerve segment (Fig. 3a–c and Table S1) and the corresponding DRG tissues (Fig. 4a–c and Table S1) of rats who had suffered a sciatic nerve defect (10 mm) and were subsequently treated with TENs, autografts, or scaffolds. The transcriptome was monitored over a series of postoperative time points (0.5 h, 1.5 h, 3 h, 6 h, 12 h, 1 d, 4 d, 1 w, 2 w, 3 w, 4 w, 8 w and 12 w for regenerative nerve segments; 0.5 h, 1.5 h, 3 h, 6 h, 12 h, 1 d, 4 d, 1 w, 2 w, 3 w and 4 w for DRG tissues). The corresponding samples from normal DRG tissues of animals not undergoing surgery served as controls.

Principal component analysis (PCA) was used in sample analysis for 3D visualization (Fig. 3d–f and 4 d-f). The analysis was focused on the 15 % of probes with the highest difference in expression among various postoperative time points and absolute expression values over 128 for at least one of the datasets (Table S2). Unsupervised hierarchical clustering (Fig. 3g–i and 4g-i) and Euclidean distance (Fig. 3k-l and 4k-l) were used to classify the expression of these 15 % of probes with striking demarcation.

In regenerative nerve segments, PCA (Fig. 3d–f) and hierarchical clustering (Fig. 3g–i) revealed that postoperative neuroregeneration segregated into four transcriptionally distinct phases for each method of treatment (TEN, autograft and scaffold). In the TEN group, phase I ranged from 0.5 h to 3 h, phase II from 6 h to 1 d, phase III from 4 d to 1 w, and phase IV from 2 w to 12 w. In the autograft group, phase I and phase II were similar to those of the TEN group; phase III corresponded to the period between day 4 and week 4, and phase IV lasted from 8 w to 12 w. In contrast to the two groups described above, rats in the scaffold group showed phase I from 0.5 h to 1.5 h; phase II from 3 h to 1 d; phase III from 4 d to 1 w; and phase IV from 1 w to 12 w. The magnitude of the transcriptional changes post-surgery was obviated by plotting the cumulative Euclidean distance amongst different samples (Fig. 3k-l). Different transitions in gene expression profiles were observed in TEN, autograft, and scaffold groups, namely, at 3 h, 1 d, and 2 w in the TEN group; 3 h, 1 d, and 1 w in the autograft group; and 1.5 h, 1 d, and 1 w in scaffold group. The number of differentially expressed transcripts was analyzed at each transition (Fig. S15a and Table S3).

In the DRG tissues, the collective data suggested a similarity in the gene expression profiles between the TEN and autograft groups. Similar to the nerve segments, the post-PNI period was also segregated into 4 different phases: phase I from 0 to 3 h, phase II from 6 to 12 h, phase III from 1 to 4 d, and phase IV from 7 d to 4 w. These phases were separated by 3 nodal transmissions at 3 h, 1 d, and 4 d. The identified genes were differentially expressed according to pairwise comparisons performed for each time point post-surgery (Fig. S15b and Table S3). The time point of 1 d was a clear transition in the postoperative time-series, in accordance with the results of PCA, hierarchical clustering and the Euclidean distance, as described above. Thus, the relationships among gene

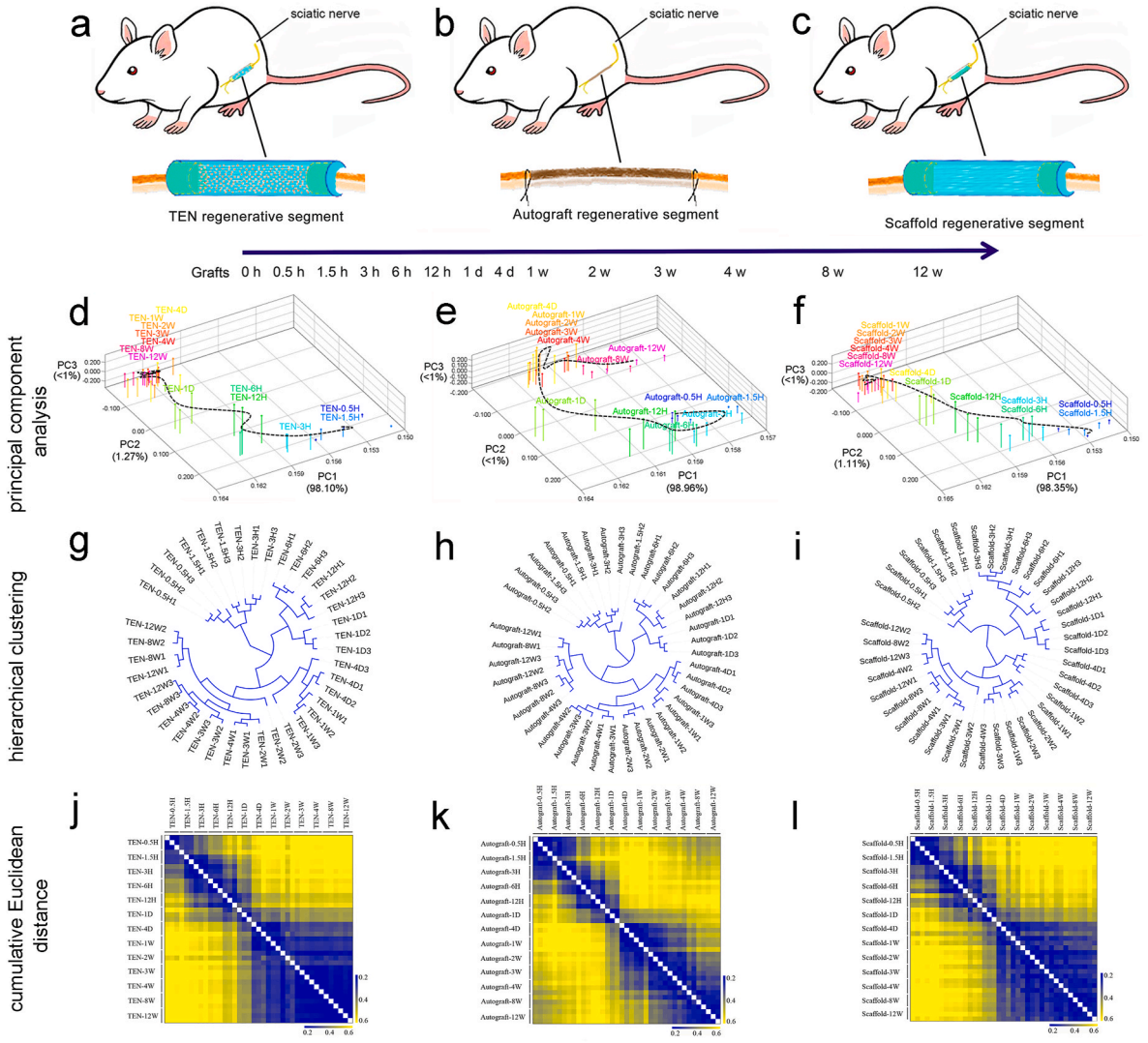

Fig. 3. | Overview of transcriptomic features in regenerative nerve segments following various repairing ways. Schematic illustration of sciatic nerve regenerative model repaired by TEN (a), autograft (b), and scaffold (c). The regenerative segments were obtained post various time points to investigate gene expression profiling. Principal Component Analysis (PCA) of TEN (d), autograft (e), and scaffold (f) group indicated samples post-surgery. Dotted curves represented macroscopic change of the indicated samples which were described above. Unsupervised hierarchical clustering among TEN (g), autograft (h), and scaffold (i) group indicated samples showed that there was different classification of the grafted segment according to similarity of probe expression profiles. Euclidean distance among TEN (j), autograft (k), and scaffold (l) group showed the different transitions of probe expression profiles.

expression profiles supported the presently accepted regenerative progression of TEN, autograft, and scaffold-aided peripheral neuroregeneration and new transcriptional insights were gained regarding each phase and the transitions.

2.5. *Distinct gene expression and interactive networks define phases of axonal regeneration in regenerated nerve segments*

To explore key functional genes related to axonal regeneration post-surgery, the average expression profile of functional genes (Z-score) for axonogenesis, as well as axon guidance, elongation, branching, growth, and regeneration were obtained (Fig. 5a–f). The results indicated that these key biological processes related to axonal regeneration shared similar transitions (6 h, 4 d and 3 w) as the average expression trends. Thus, 4 phases designated “injury response phase”, “molecular regeneration phase”, “morphological regeneration phase” and “remodeling phase” were identified. The time points of 6 h, 4 d and 3 w were regarded as the initiation of “molecular regeneration phase”, “morphological regeneration phase” and “remodeling phase” respectively.

To further clarify the interaction among proteins encoded by the functional genes for axonal regeneration, protein-protein interaction (PPI) networks were constructed by a database of ingenuity pathway analysis (IPA). Cascade PPI networks involved in the guidance and outgrowth of axons were selectively depicted (Fig. 5g–i and Fig. S2). The cascade PPI networks clearly showed their molecular types (i.e., cytokine, phosphatase, enzyme, kinase, ion channel, peptidase, transcriptional regulator, translation regulator, transmembrane receptor, transporter, etc.) through their dynamic changes of mRNA expression. The response to PNI leads to dysregulation of genes essential for guidance and outgrowth of axons. In the TEN group, we noticed repression of two early response genes, FOS and EGR2 (also named KROX20), both of which are associated with the branching and guidance of axons. These genes are also involved in cell proliferation, differentiation, transformation and anti-apoptotic signaling [27–31], indicating that immediate-early response is inhibited by TEN implantations. qPCR results verified the differential expression of these genes, including FOS, SEMA3E, TGFβ1, NRG1, VAX2 and EGR2, associated with axonal regeneration (Fig. 5j-o). The above-described genes could be important

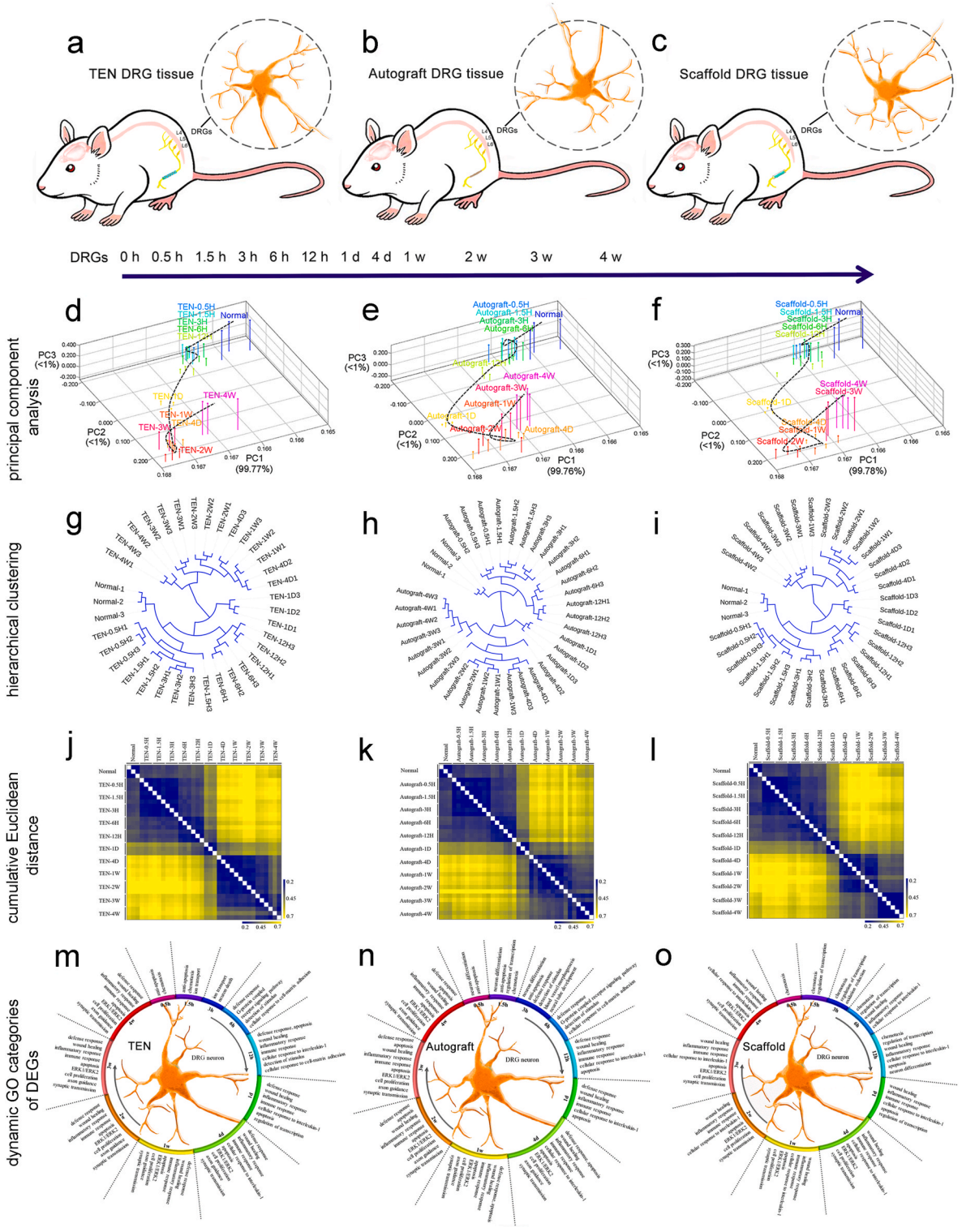

Fig. 4. | Overview of transcriptomic features in the DRG tissues corresponding to sciatic nerve following various repairing ways. Schematic illustration of sciatic nerve regenerative model repaired by TEN (a), autograft (b), and scaffold (c). The DRG tissues were obtained post various time points to investigate gene expression profiling. Principal Component Analysis (PCA) of TEN (d), autograft (e), and scaffold (f) group indicated samples post various time points. Dotted curves represented macroscopic change of the indicated samples which were described above. Unsupervised hierarchical clustering among TEN (g), autograft (h), and scaffold (i) group indicated samples showed that there was different classification of the DRG tissues according to similarity of probe expression profiles. Euclidean distance among TEN (j), autograft (k), and scaffold (l) group indicated samples owned the different transitions of probe expression profiles. The enriched gene function annotation analysis showed the dynamic GO categories of DEGs among TEN (m), autograft (n), and scaffold (o) group.

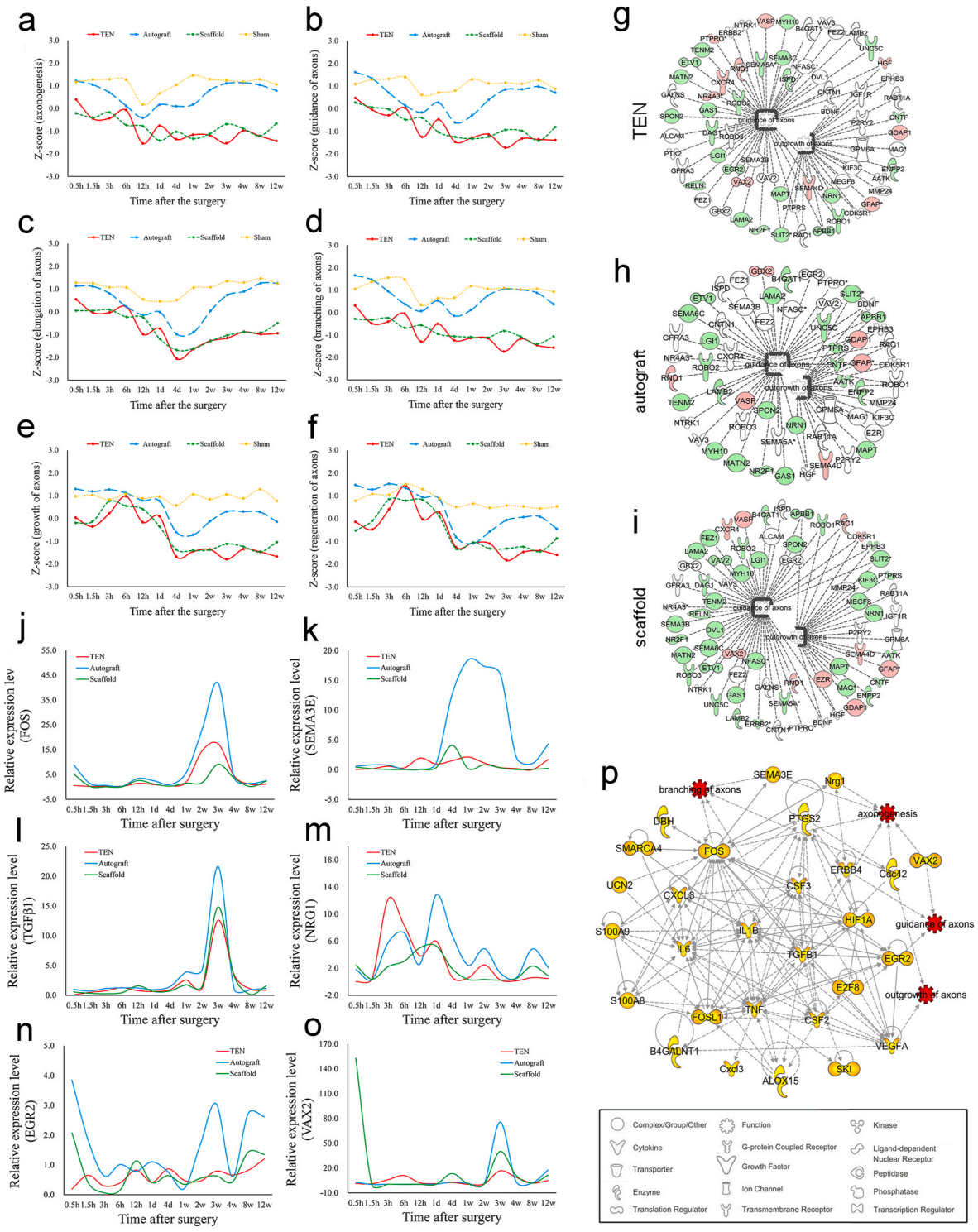

Fig. 5. | Distinct gene expression and interactive networks of axonal regeneration in regenerative nerve segments. The average expression profiles (Z-scores) of functional genes involved in axonogenesis (a), guidance of axons (b), elongation of axons (c), branching of axons (d), outgrowth of axons (e) and regeneration of axons (f) at different time points post-surgery were calculated in TEN (red), autograft (blue), scaffold (green) groups and sham group (yellow). The protein-protein interaction (PPI) networks of TEN (g), autograft (h), scaffold (i) groups involved in the guidance and outgrowth of axons at 6 h post-surgery was selectively depicted by a database of ingenuity pathway analysis (IPA). The PPI networks clearly showed their molecular types and interactions (i.e., cytokine, phosphatase, enzyme, kinase, ion channel, peptidase, transcriptional regulator, translation regulator, transmembrane receptor, transporter, etc.). qPCR results verified the differential expression of these genes, including FOS (j), SEMA3E (k), TGFβ1 (l), NRG1 (m), EGR2 (n), and VAX2 (o), associated with axonal regeneration. To summarize the molecular effects on peripheral nerve regeneration, a specific network for axonal regeneration was constructed (p).

in affecting axonal regeneration after PNI. To summarize the molecular effects on peripheral nerve regeneration, a validated and specific network for axonal regeneration was constructed (Fig. 5p).

2.6. Transcriptomic analysis of remyelination implicates specific molecules and interactive networks in regenerative nerve segments

To screen crucial genes related to remyelination post-surgery, Z-score for differentiation of SCs, proliferation of SCs, chemotaxis of neuroglia, migration of SCs, myelination of axons, myelination of SCs, formation of the myelin sheath and thickness of the myelin sheath were obtained (Fig. 6a–h). The results indicated that these key biological processes related to myelination shared similar transitions (6 h, 4 d and 3 w) with the principal average expression trends. Thus, 4 distinct phases were designated as “injury response phase”, “molecular myelination phase”, “morphological myelination phase” and “remodeling phase”. Concretely, the “injury response phase” was mainly enriched in biological processes, such as dedifferentiation and proliferation of SCs. The “molecular myelination phase” was enriched for chemotaxis of neuroglia and migration of SCs. The “myelination phase” was enriched for myelination of axons and SCs, formation of myelin sheaths; “remodeling phase” was enriched for thickness and compaction of myelin sheath (Figs. S3a–c).

To further clarify the relationships among proteins encoded by the functional genes for remyelination, cascade PPI networks involved in the differentiation, proliferation, migration, myelination of SCs, myelination of axons, formation of myelin sheaths and regulation of myelin sheath thickness were selectively depicted (Fig. 6i–k and Fig. S6). The qPCR results verified that the differential expression of the genes, including SMARCA4, CAMK2B, IL6, SKI, CDC42 and ERBB4, were essential in affecting myelination after PNI (Fig. 6i-q). To summarize the molecular effects on remyelination during peripheral nerve regeneration, a validated and specific network for myelination was constructed (Fig. S15c).

2.7. Transcriptomic analysis of vascularization implicates specific molecules and interactive networks in regenerative nerve segments

To discover core genes related to vascularization post-surgery, Z-score indicating vascular endothelial cell (VEC) behavior (activation, differentiation, proliferation, chemotaxis, adhesion, migration, sprouting, and tubulation), angiogenesis, lymphangogenesis, the branching and remodeling of blood vessels were obtained (Fig. 7a–i). The results indicated that these key biological processes related to vascularization shared similar transition points (6 h, 4 d and 8 w) in their average expression trends. Thus, 4 phases were designated as “injury response phase”, “molecular vascularization phase”, “morphological vascularization phase” and “remodeling phase”. The “injury response phase” was enriched for enriched for the biological processes of activation, differentiation, and proliferation of VECs; the “morphological vascularization phase” was enriched for angiogenesis, sprouting of VECs, tubulation of VECs, and branching of blood vessels; and the “remodeling phase” was enriched for remodeling of blood vessels (Fig. S4m). The dynamic mRNA expression profiles in lymphangogenesis during peripheral nerve regeneration were also reported (Fig. 7i).

To further investigate the relationships among the proteins encoded by functional genes for vascularization, cascade PPI networks were constructed by IPA, which involved in activation, cell proliferation, adhesion, chemotaxis, migration, sprouting and tubulation of VECs, branching and remodeling of blood vessels, and lymphangiogenesis (Fig. 7m-r, Figs. S7 and S8). qPCR results verified that the differential expression of the genes, including TNF, CSF2, IL1B, PTGS2, S100A8, HIF1A, DBH, ALOX15, E2F8, S100A9, FOSL1, and VEGFA were indispensable in affecting vascularization during neuroregeneration (Figs. S4a–i). The VEGFRA, E2F8, SEMA3E and CSF1 were proved to co-localize with VECs (RECA1 positive) by Immunohistofluorescence chemical staining (Fig. S4n).

To summarize the molecular effects on vascularization during peripheral nerve regeneration, a validated and specific network for vascularization was constructed (Fig. S15d).

2.8. Phase-specific differentially expressed genes drive apoptosis and axonal regeneration by remodeling gene regulatory networks in DRG tissues

PNI initiates significant changes of gene expression in DRGs that induce the increased inherent regenerative capability [32]. However, a key issue that remains to be further realized is how bridging with TEN affects the inherent regenerative capability of DRG neurons after PNI, especially for a nerve gap. Thus, to investigate the regulation of the functional genes related to apoptosis and axonal regeneration in DRG tissues post-surgery, Z-score for apoptosis of neuroglia and neurons, axonogenesis, and guidance, elongation, branching, outgrowth, and regeneration of axons were obtained. Changes in expression shared similar transitions in the average expression trends for apoptosis (3 h, 1 d and 1 w) and axonal regeneration (6 h, 1 d and 2 w) (Fig. 8a–h). For the regulation of apoptosis, four phases were designated to describe the process including the “injury response phase”, “molecular apoptosis phase”, “morphological apoptosis phase” and “post-apoptosis phase” based on the average expression of functional genes for apoptosis of neuroglia and neurons. Moreover, for the regulation of axonal regeneration, four phases were designated to describe the process including “injury response phase”, “molecular regeneration phase”, “morphological regeneration phase” and “post-regeneration phase”.

The cascade PPI networks involved in apoptosis of neuroglia and neurons were selectively depicted to further clarify the relationships among the proteins encoded by the functional genes for apoptosis and axonal regeneration (Fig. 8i-n, Figs. S9–10). The qPCR results verified that the differential expression of selected genes including TNFAIP6, GAL, FOS, CCL2, NFKBIA, CDKN1A, CCK, and CSF1 was associated with apoptosis and axonal regeneration (Fig. 8o–v). Furthermore, the protein expression of the selected genes, including TNFAIP6, CCL2, GAL, NFKBIA, CCK and CSF1, was also validated by Western blot (Figs. S5a–g). We hypothesized the above-described genes could be important for affecting apoptosis of neuroglia and neurons in DRG tissues following PNI. To summarize the molecular effects on apoptosis of neuroglia and neurons during peripheral nerve regeneration, specific networks for apoptosis and axonal regeneration were constructed, respectively (Figs. S15e–f).

We selected eleven candidate genes (Ankrd1, Sbno2, Cdkn2a, Crem, Hoxb8, Zfp488, Zfp36, Gfi1, Esr2, Nfkbia, Csrnp1) involved in apoptosis and axonal regrowth for further validation. However, the TUNEL assays failed to show the positive effect on the apoptosis of adult DRG neuron model *in vitro,* which best mimic the peripheral nerve injury. None significant differences were detected between candidate genes knockdown group and control group (Data not added in the revised manuscript). Furthermore, primary cultured adult DRG neurons were infected with RNAi lentivirus targeting Ankrd1, Sbno2, Cdkn2a, Crem, Hoxb8, Zfp488, Zfp36, Gfi1, Esr2, Nfkbia, Csrnp1 or negative control (Genepharma, Shanghai, China), respectively, the maximum length of neurites (longer than its soma diameter) of each neuron were measured and analyzed. In a word, the RNAi lentivirus targeting all above eleven genes significantly inhibit the axonal regrowth of DRG neurons except Cdkn2a and Zfp488 (Fig. S16).

2.9. Distinct transcriptional regulators (TRs) shape the transcriptomic landscape during neuroregeneration in DRG tissues

TRs generally initiate specific signaling pathways or biological processes [33]. To investigate the dynamic changes of the TRs in DRG tissues post-surgery, the expression levels of TRs were quantified and are shown in the clustered heat maps and compared to normal controls at

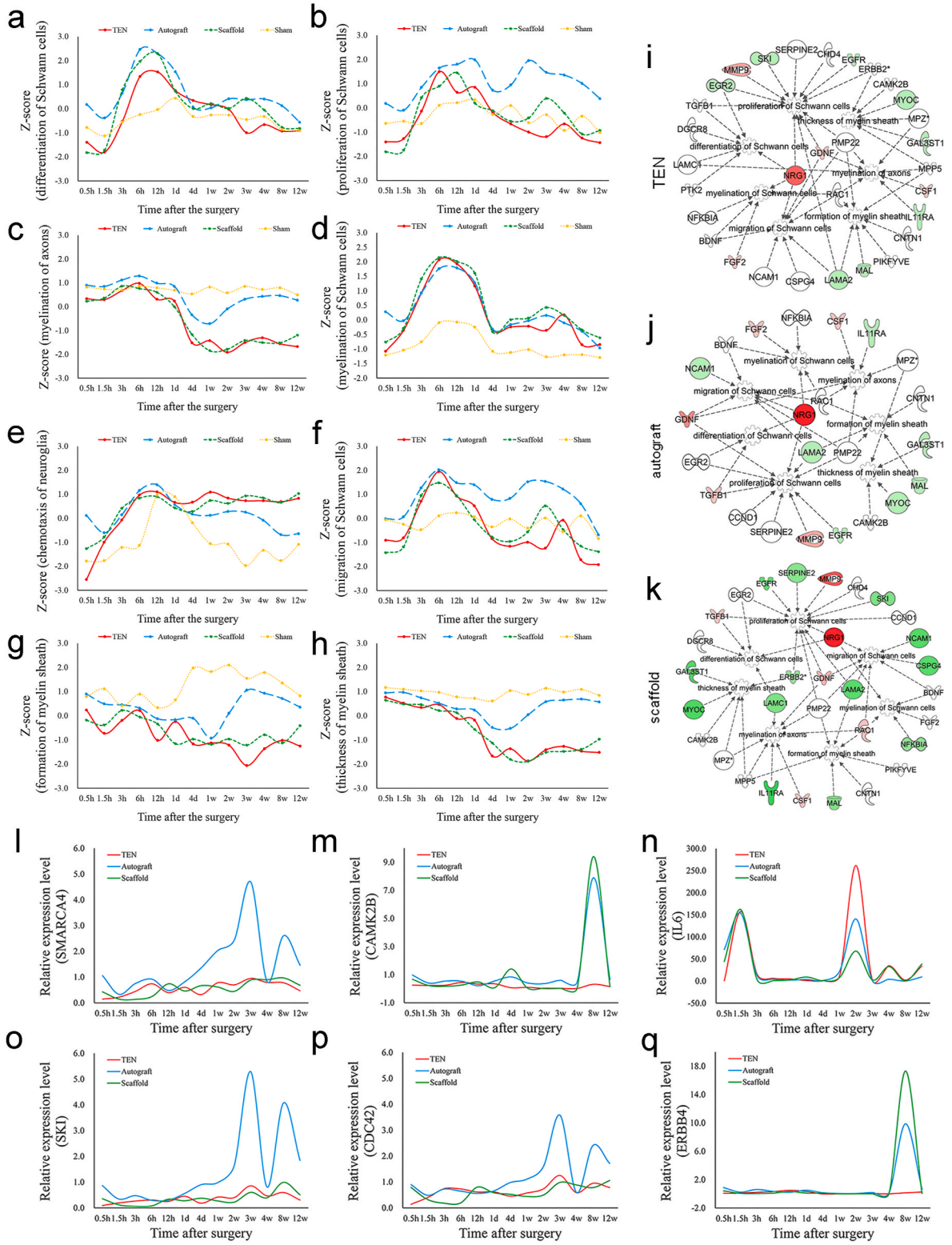

Fig. 6. | Distinct gene expression and interactive networks of myelination in regenerative nerve segments. The Z-scores of functional genes involved in differentiation of SCs (a), proliferation of SCs (b), chemotaxis of neuroglia (c), migration of SCs (d), myelination of axons (e), myelination of SCs (f), formation of myelin sheath (g) and thickness of myelin sheath (h) at different time points post-surgery were calculated in TEN (red), autograft (blue), scaffold (green) groups and sham group (yellow). The PPI networks of TEN (i), autograft (j), scaffold (k) groups involved in above described functions were selectively depicted at 6 h post-surgery. The qPCR results verified that the differential expression of the genes, including SMARCA4 (l), CAMK2B (m), IL6 (n), SKI (o), CDC42 (p) and ERBB4 (q), were essential in affecting myelination post-surgery.

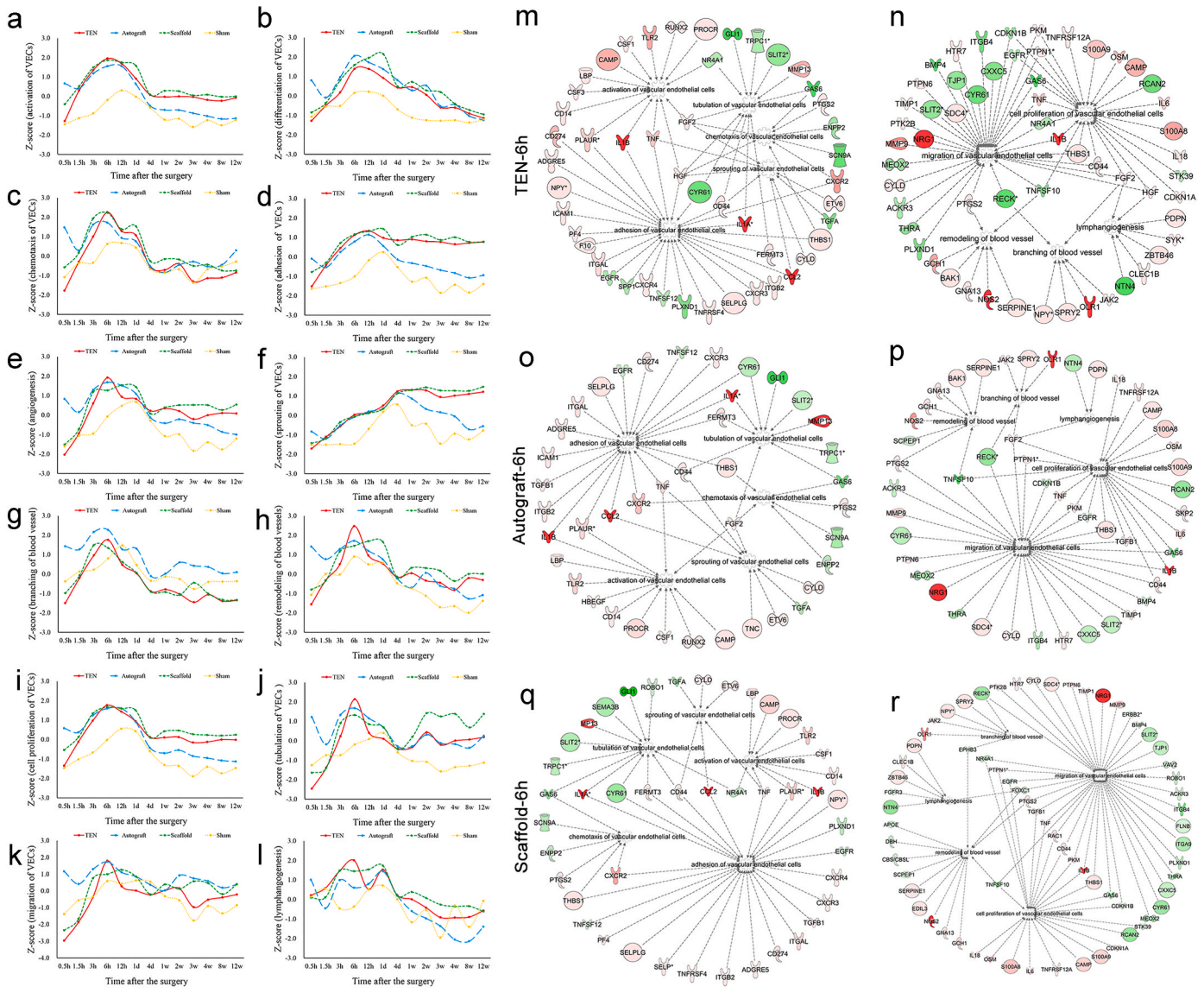

Fig. 7. | Distinct gene expression and interactive networks of vascularization in regenerative nerve segments. The Z-scores of functional genes, which were involved in activation of VECs (a), differentiation of VECs (b), chemotaxis of VECs (c), adhesion of VECs (d), angiogenesis (e), sprouting of VECs (f), branching of blood vessel (g), remodeling of blood vessel (h), cell proliferation of VECs (i), tubulation of VECs (j), migration of VECs (k), and lymphangogenesis (l) at different time points post-surgery were calculated in TEN (red), autograft (blue), scaffold (green) groups and sham group (yellow), respectively. The PPI networks of TEN (m, n), autograft (o, p), scaffold (q, r) groups involved in above described functions were selectively depicted at 6 h post-surgery.

0.5 h, 1.5 h, 3 h, 6 h, 12 h, 1 d, 4 d, 7 d, 1 w, 2 w, 3 w and 4 w following surgery (Fig. S14). To further investigate the dynamic interactions among TRs, cascade PPI networks were also constructed by IPA (Figs. S12a–c). Venn diagrams show the number and overlap of differentially expressed TRs in the TEN, autograft, and scaffold groups compared with the control group at 0.5 h, 1.5 h, 3 h, 6 h, 12 h, 1 d, 4 d, 7 d, 1 w, 2 w, 3 w and 4 w post-surgery (Fig. S13). In our work, TRs including CMTM2A, SP2, PURA and EGR2, were involved in initiating the subsequent signaling cascades at 0.5 h post-surgery. We focused on the highly expressed and multifunctional TRs, which may be more important than other TRs. Therefore, ATF3, JUN, Cmtm2a, HES5, CDKN2A, and ERG2 were selected for further qPCR (Figs. S14a–f) and Western blot validation (Fig. 14g–j). The number of TRs in the TEN and autograft groups significantly increased after 1 d and were maintained at a high level until week two, after which they decreased during week three and four (Figs. S12a–c). The same increase in TRs was not observed in the scaffold group. To summarize the molecular changes in TRs, a validated and specific network was constructed (Fig. S14k).

3. Discussion

Over the past decades, stem cells originate from various tissues or organs as bone marrow, blood, adipose tissue, hair follicles, placenta and epidermis have been explored in quite a few preclinical studies, and even clinical trials [24,34–36]. However, no stem cells have been approved as products for the treatment of PNI. The development of SKPs and their differentiated successors (SCs and neurons) provides a new source that could be applied for PNI therapy [17–19,37]. In this work, we manipulated SKP-SCs for the construction of TENs *in vitro* using the RCCMax system and applied the TENs in an acute rat sciatic nerve defect model. Extensive behavioral, electrophysiological, histological evaluation of regenerated nerves and reinnervated target muscles jointly demonstrated that both nerve regeneration and target muscle reinnervation were highly improved in the TEN and autograft groups. The TEN group reached that observed in the autograft group with no significant difference in all parameters of nerve regeneration. Our endeavors to fabricate TENs *in vitro* utilizing SKP-SCs and their ECM components were

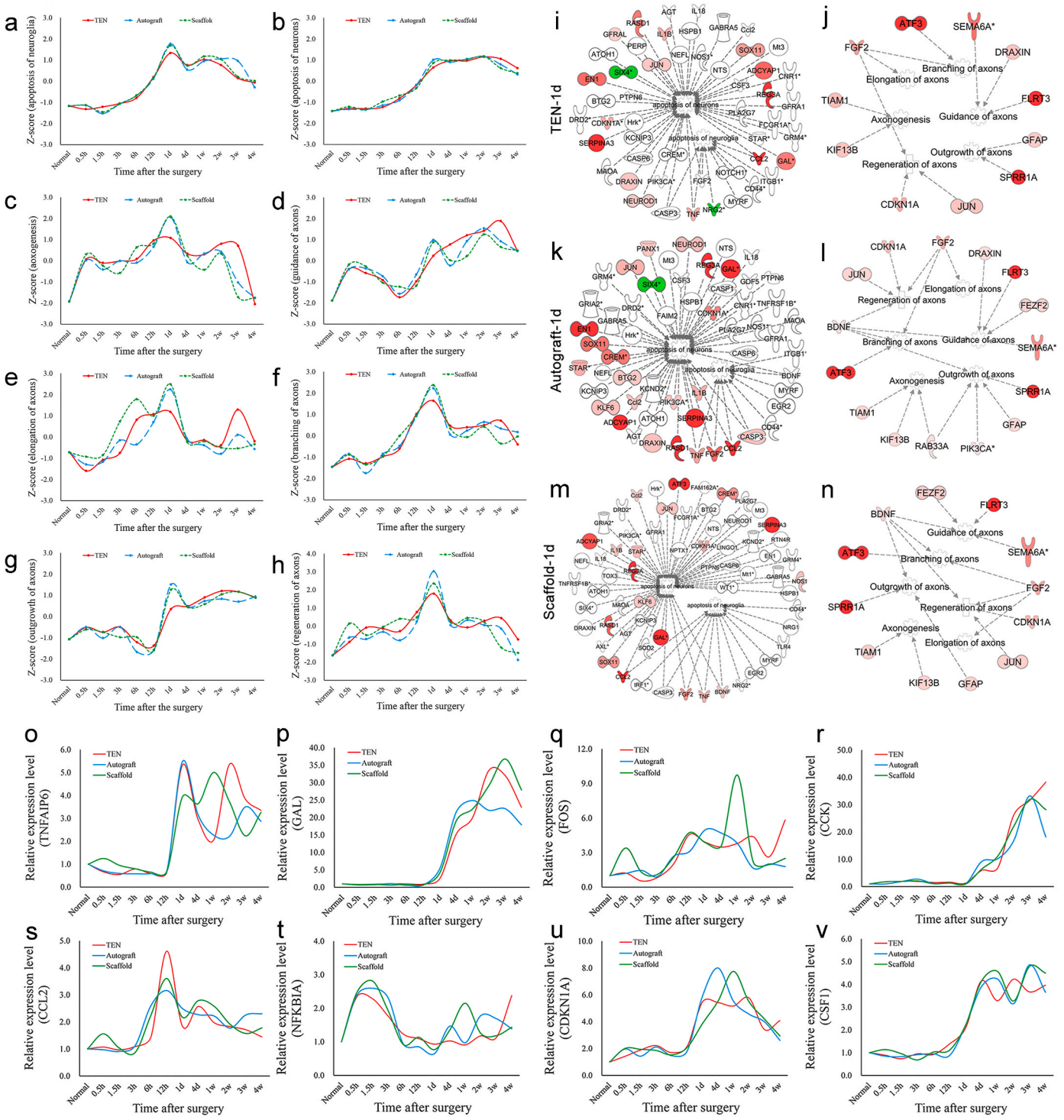

Fig. 8. | DEGs drive apoptosis and axonal regeneration by remodeling gene regulatory networks in DRG tissues. The average expression profiles (Z-scores) of functional genes involved in apoptosis of neuroglia (a), apoptosis of neurons (b), axonogenesis (c), guidance of axons (d), elongation of axons (e), branching of axons (f), outgrowth of axons (g), and regeneration of axons (h) at different time points post-surgery were calculated in TEN (red), autograft (blue), and scaffold (green) groups, respectively. The PPI networks of TEN (i, j), autograft (k, l), scaffold (m, n) groups involved in above described functions were selectively depicted at 1 d post-surgery. The qPCR results verified that the differential expression of selected genes including TNFAIP6 (o), GAL (p), FOS (q), CCK (r), CCL2 (s), NFKBIA (t), CDKN1A (u), and CSF1 (v) was associated with apoptosis and axonal regeneration.

motivated by the thought of prolongating the effect of support cells and their bioactive cues that promote peripheral nerve regeneration as much as possible. However, entirely restoration of neural functionality remains a leading challenge.

Two key determinants of effective nerve regeneration are well known as an inherent growth ability and a superior external microenvironment [38–40]. Following PNI, neurons initiate series of dynamic molecular changes in answer to bioactive cues in local microenvironment [41] and tend to regrow new axons [42]. TRs and their cascade networks could be interactive according to the regenerative program by

regulating the gene expression in injured neurons [43–45]. The initiation of inherent growth ability is determined by the local bioactive microenvironment, which consists of various concerted signals organized by SCs, macrophages, fibroblasts, and inflammatory cells in the regenerative microenvironment [38,40,42,44,46]. Successful neuroregeneration requires the synchronized activity of several interactive systems. The complexity rising from current research addresses the importance of proposing a novel theoretical outline, involving various parallel processes that go astray following PNI. We described our current understanding of the injury-inducible transcriptional regulators that enhance peripheral nerve regeneration, and provided a platform to recruit injury-inducible transcription factors, in simultaneous gene regulation. In the PNS, nerve injury signals from the permissive environment are transduced via cell surface receptors of the cell body and via retrograde axonal transport. Ultimately, the signals are integrated into specific regulators of the nuclear transcription factors that induce the expression of large ensembles of distinct genes sequentially and under tight control. Thus, for successful clinical translation of the TENs, further research into the mechanisms by which the TENs regulate peripheral nerve regeneration is essential.

Here, we engineered a regenerative microenvironment using TEN to bridge and evaluate the functional recovery of injured sciatic nerves in rats. Based on our experiences and previous work, cell laden conduit owned some limitations as leakage of seed cells and low survival rate after transplantation. Although the SKP-SCs and silk/chitosan-based conduits were previously reported, we prepared a chitosan/silk fibroin neural scaffold with a perfusion bioreactor (RCCMax system) to fabricate the standardized TEN efficiently, which continuously provided oxygen and nutrition while removing metabolites (Fig. 1d and Movie S1). Moreover, the ascorbic acid was added to stimulate the secretion of extracellular matrix (collagen I, collagen IV, fibronectin and laminin) within one week after SKP-SCs attached to the surface of the neural scaffold (Fig. 1f), which provided a permissive surface and microenvironment to support axonal regeneration. Therefore, the above described limitations were avoided to some extent via our design in the present work. For achieving better effect of neuroregeneration, this is the first time to jointly apply a dynamic perfusion bioreactor and the ascorbic acid to stimulate the SKP-SCs secretion of extracellular matrix.

We also illustrated the current understanding of the injury-induced genes that improve peripheral nerve regeneration. To realize the comprehensive gene regulation processes that determine the peripheral nerve regeneration, a large-scale screening approach using microarrays was used to identify a series of injury-induced genes. Due to the core of peripheral nerve regeneration is the outgrowth of axons, we additionally explored the regulation of genes associated with axonal regeneration. During the stress response phase, the regrowth of neurites/axons had not yet been induced as only a few genes associated with regrowth showed increased expression. From the “pre-regeneration phase” to the “regeneration phase”, however, more genes associated with neurite/axon growth, including ATF3, CDKN1A, IL6, IGF1, FGFR3, RUNX3, JUN, SOCS3 and AGTR2, NPY, PLD2, GNA15, GAP43, CSF1, RHOQ, and PRAD, were gradually upregulated. Importantly, these genes have proven to be useful in promoting nerve regeneration.

SCs can migrate along the surface of polarized blood vessels that guide SCs and axons through the matrix in the nerve gap [47]. Thus, due to the importance of vascularization in the clinical application of tissue-engineered products and various strategies that have been considered to obtain functional networks of blood vessels in regenerative tissue [48], it is essential to clarify the transcriptomic features of a regenerated vascular network in engineered neural tissue. To engineer vascular tissues or induce vascularization from preexisting blood vessels and capillaries, one must understand the molecular mechanisms of blood vessel formation *in vivo*. Another mechanism of blood vessel formation is through the sprouting of existing blood vessels, a process known as angiogenesis [48]. Vascularization is currently regarded as one of the main challenges inhibiting further large-scale clinical applications [49,50]. Only a few engineered tissues, including skin, cartilage, and bladder tissue, have achieved clinical success. Thus, the generation of functional vascular grafts is essential for the clinical success of engineered tissue constructs and remains an obstacle for regenerative medicine [51]. Because vascularization is a highly organized process *in vivo*, the spatial and temporal presence of specific signaling molecules is an important aspect of the biochemical modulation using biomaterials. It is crucial for TENs to exhibit properties that mimic the *in vivo* complexities of blood vessel formation. After implantation of the TEN, spontaneous vascularization of the implant is usually observed due in part to the local inflammatory response. The seeded cells often create a hypoxic environment in the implant that stimulates the endogenous release of angiogenic growth factors. Morphologically, specialized endothelial cells, called tip cells, with numerous dynamic filopodia, comparable to axonal growth cones, localize at the angiogenic front, and actively detect molecular cues in their surroundings [52,53]. Mechanistically, the guidance systems of vessels and nerves shares common underlying signaling pathways [46,53–58]. Some axon guidance molecules, such as netrins, ephrins, slits, semaphorins, Nogo receptors, and Eph receptors, are also pro- or anti-angiogenic factors [46,53,54,56,58–60].

We eventually validated the candidate genes involved in axonal regrowth. Sbno2, Crem, Hoxb8, Zfp36, Gfi1, Esr2, Nfkbia, Csrnp1 were firstly reported their roles in axonal regrowth of DRG neurons (Fig. S16). The role of Ankrd1 was proved in accordance with previous work [61] that indicated our data were worthy of scrutiny and reliability.

In summary, we systematically analyzed specific molecules and signaling pathways during the biological processes of cell apoptosis, axon regeneration, myelination and revascularization after repairing peripheral nerve defects with TEN, autograft and neural scaffold, respectively. Our work illustrates the overall variation in main regenerative biological processes, related core genes, and their interactive networks (Graphic Abstract). The TEN constructed using SKP-SC and chitosan/silk filament scaffolds was demonstrated to improve peripheral nerve regeneration and functional restoration. The transcriptomic and bioinformatics data revealed complex molecular networks and orchestrated functional regulation that may be liable for the effects of TEN on improving peripheral nerve regeneration. This work sets the stage for future studies in primates and clinical trials to investigate the potential of biosafety and effectiveness in the management of peripheral nerve defects.

Over the past decade, considerable insights into the molecular mechanisms driving the recovery of PNI have suggested new therapeutic targets and provided scientific rationale for future clinical trials. Recognition of the complexity of the peripheral nerve regenerative process, as well as acceptance of the related pathological changes will be a critical step in these future efforts. Consequently, the combination of our current knowledge in neurobiology, the identification of the limits of past clinical trials as well as translational research and more accurate therapy will provide a strong basis to advance viable clinical approaches for treating patients with PNI.

4. Materials and methods

4.1. Animals

After approval of the research protocol by the Administration Committee of Experimental Animals, Jiangsu Province, China [SYXK (Su) 20190225-004], newborn (1–3 d), embryonic (E14 d) and adult (weight 220 g–250 g) Sprague Dawley (SD) rats were purchased from the experimental animal center of Nantong university. The anesthesia of adult female SD rats was under intraperitoneal injection of 3 % sodium pentobarbital solution according to 30 mg/kg of body weight. All experiments involving animals were performed in accordance with the US National Institute of Health (NIH) Guide for the Care and Use of Laboratory Animals published by the US National Academy of Sciences.

4.2. Isolation of SKPs and their induced differentiation into SKP-SC

SKPs were isolated from the backs of 1 to 3-day-old Sprague Dawley and green fluorescent protein (GFP)-transgenic rats as previously reported with minor modification [22]. Backs were firstly waxed and cleaned with ethanol before a patch of skin was removed. The skin was cleaned of fat, fascia, and blood vessels and minced into small pieces a few millimeters in size with razor blades. Minced skin was digested in collagenase type XI (1 mg/ml), inverting at 37 °C for 1.5–2 h. Intermittent mechanical mashing was done with a 10 ml pipette every 40 min. Digested skin was triturated with a P1000 pipette and diluted with DMEM to stop digestion. The skin solution was filtered by a 40 μm cell strainer (BD Falcon, Bedford, MA, USA) to remove undigested skin and collect only single cells. Single cells were grown in "SKPs proliferation media" which contained DMEM/F12 (3:1), 1 % penicillin/streptomycin, 2 % B27 supplement (Invitrogen, Carlsbad, CA, USA), 20 ng/ml EGF, and 40 ng/ml FGF-2 (BD Bioscience, San Diego, CA, USA). To prevent contamination from dissection, 1 μg/ul Fungizone Antimycotic was added. The cells were seeded from 25 000 to 50 000 cells/ml media in a vented-cap flask. SKPs were fed with SKPs proliferation media every 5 days and passaged when floating spheres turned largely. To passage SKPs, the spheres were separated from the conditioned media by centrifugation. Conditioned media filtered through a 20 μm syringe filter was saved for feeding. Spheres were digested with 1 mg/ml collagenase for 10 min in a 37 °C water bath, followed by trituration with P1000 and P200 pipettes. Dissociated spheres were resuspended in SKPs proliferation media that contained half DMEM/F12 (3:1) and half conditioned media.

SKP-SCs were differentiated from passage three SKPs as previously described [17,22]. SKPs were dissociated to single cells, as during passaging. Single cells were resuspended in "SKP adherence media" containing DMEM/F12 (3:1), 1 % penicillin/streptomycin, 10 % fetal bovine serum (FBS, HyClone, Logan, UT, USA), 1 % B27 supplement, 1 % N2 supplement, 20 ng/ml EGF, and 40 ng/ml FGF-2. Cells were plated at 25 000 cells/ml in petri dishes. After 3 days, the media was changed to SC proliferation media and was replenished every 3–4 days. SC colonies that could be seen after 2–3 weeks were isolated with cloning cylinders (Corning). When confluent, cells were expanded and passaged with trypsin-EDTA (Thermo Fisher Scientific, Carlsbad, CA, USA).

4.3. Immunocytochemistry

To check for the expression of typical SKP and SC markers, immunocytochemistry was achieved. After fixed in 4 % paraformaldehyde for 10 min, cells were blocked with 5 % normal goat serum and permeabilized with 0.1 % Triton-X for 30 min. Primary antibody was incubated overnight at 4 °C, followed by a secondary antibody incubation for 2 h at room temperature. Where Hoechst was used, 1:5000 Hoechst 33342 (Sigma-Aldrich, St. Louis, MO, USA) was added for incubating 5 min. The following primary antibodies were used at the stated dilutions: mouse anti-nestin antibody (1:200, Millipore, Temecula, CA, USA), rabbit anti-Sca-1 (1:200, Merck Millipore, Darmstadt, Germany), rabbit anti-versican, fibronectin, vimentin, collagen I, collagen IV (1:200, Abcam, Cambridge, MA, USA), chicken anti-P0 (1:500, Aves Labs, Davis, CA, USA), mouse anti-S100β and anti-laminin (1:500, Sigma Aldrich, St Louis, MO, USA), rabbit anti-GFAP (1:500, Dako, Tokyo, Japan), mouse anti-$p75^{NTR}$ (1:500, Chemicon, Temecula, CA, USA), mouse anti-NF200 (1:400, Abcam, Cambridge, MA,USA), and rabbit anti-MBP (1:500, Millipore, Billerica, MA, USA). The following secondary antibodies were used at the stated dilutions: Alexa 555 goat anti-chicken, Alexa 555 goat anti-rabbit, Alexa 488 goat anti-mouse, Alexa 555 goat anti-mouse, (all 1:1000, all Invitrogen, Carlsbad, CA, USA).

4.4. Myelination of DRG axons in vitro

In vitro myelination of SKP-SC was assessed using the DRGs myelination assay [62]. DRGs were isolated from E14.5 SD rats and dissociated with 0.25 % trypsin. Dissociated ganglia were plated at 300 000 cells/ml on Matrigel and poly-D-lysine (Sigma) coated chamber slides in "axon growth media" containing 2 % B27 supplement, 1 % GlutaMAX supplement, 50 ng/ml NGF, and 1 % penicillin/streptomycin in Neurobasal media. Media was changed every other day. To obtain pure axons cultures, cytosine arabinoside was added to the media for one media change. One week after obtaining pure axons, SKP-SCs were added in media containing 1 % ITS supplement (Sigma-Aldrich, St. Louis, MO, USA), 1 % GlutaMAX supplement, 0.2 % bovine serum albumin, 4 g/l D-glucose (Sigma-Aldrich, St. Louis, MO, USA), 50 ng/ml NGF, and 1 % penicillin/streptomycin in Basal Media Eagle (BME, Invitrogen, Carlsbad, CA, USA). The SKP-SCs were grown in 10 % FBS in DMEM (instead of in Schwann cell proliferation media) for three days. Media was changed every other day. After 6–8 days, SCs were induced to myelinate by changing to culture in "myelination media" containing 1 % ITS supplement, 1 % GlutaMAX supplement, 15 % FBS, 4 g/l D-glucose, 50 ng/ml NGF, 1 % penicillin/streptomycin, and 50 μg/ml L-ascorbic acid (Sigma-Aldrich, St. Louis, MO, USA) in BME. Myelination media was exchanged every other day for 10–14 days. Immunocytochemistry was performed on the cultures at the endpoint for MBP, P0, MAG and NF200.

4.5. Construction of TEN in vitro

As the previous report, the chitosan/silk fibroin-fabricated neural scaffold was prepared as following [63]. According to the Chinese patent ZL 0110820.9 A, chitosan conduit was fabricated of chitosan gel by injection molding, and silk fibers (*Bombyx mori* silk) were processed by degumming in aqueous boiling Na_2CO_3 solution. Then, a chitosan/silk fibers (SFs)-fabricated neural scaffold was obtained by inserted 120 of SFs in a chitosan conduit. SKP-SCs were seeded to the neural scaffold at a cell density of 1×10^7 cells/ml. The culture was transferred to a perfusion rotatory cell culture system (RCCMax) (Synthecon Inc, Friendswood, TX) 24 h later to facilitate continuous incubation for seven days with the addition of fresh ascorbic acid (50 μg/ml, Sigma, St. Louis, MO, USA) and 15 % FBS (Fig. 1d) to stimulate ECM secretion. After washed with PBS, a SKP-SCs seeded TEN was fabricated for further surgery.

4.6. Surgical procedure

After anesthesia, shaving and disinfection, a skin incision and separating nearby muscles in the left lateral thigh carried out to expose sciatic nerve were in adult female SD rats. To obtain a 10 mm long nerve defect after retraction of the nerve stumps, a 6 mm long segment of sciatic nerve was transected and removed. All rats were randomly divided into 4 groups as TEN, autograft, scaffold, and sham groups. The sciatic nerve defect was separately bridged via 3 types of nerve grafts: 1) A TEN prepared by 3D culturing SKP-SCs to a chitosan/SFs neural scaffold *in vitro*; 2) an autologous nerve graft prepared by a reversed nerve segment; 3) a chitosan/SFs neural scaffold consisting of a chitosan hollow conduit (i.d. 2.0 mm) and 120 of SFs (12 mm long, diameter 8 μm). Moreover, rats obtaining a sham surgery were considered to be the control group that underwent the same procedures without injuring the sciatic nerve.

Moreover, another treatment group of rats was subjected to the same nerve defect that bridged via GFP-SKP-SCs-containing, chitosan/SF-fabricated TENs, which were prepared using the same protocol as that used for SKP-SC-containing, chitosan/SF-based TENs but GFP-labeled cells were seeded. Each week for three weeks post-surgery, the grafting segment was obtained from rats and subjected to GFP fluorescent monitoring under microscopic observation.

4.7. Behavioral analysis

The motor functional recovery was assessed by CatWalk XT 9.0 gait analysis system (Noldus, Wageningen, Netherlands) at 4, 8, and 12 weeks post-surgery. The rats were located on the left side of a corridor with an infrared pressure sensing module and motivated to go through the corridors toward the right end that the video and data were dynamically recorded. The total toe spread (TS), intermediate toe spread (IT) and footprint length (PL) were measured via CatWalk XT 9.0 software in the injured side (E) and contralateral uninjured side (N). The sciatic function index (SFI) value was calculated by the formula of SFI = 109.5 (ETS-NTS)/NTS-38.3 (EPL-NPL)/NPL+13.3 (EIT-NIT)/NIT-8.8 that oscillates from 0 to −100, with 0 representing to normal function and −100 to complete dysfunction.

4.8. Electrophysiological assessment

To investigate recovery of nerve conduction, the sciatic nerve was re-exposed in both injured and contralateral uninjured side and we carried out electrophysiological tests in all rats 12 weeks post-surgery. The compound muscle action potentials (CMAPs) were recorded on the belly of target gastrocnemius muscle when the electrical stimuli were applied to both proximal and distal nerve stumps, respectively. The nerve conduction velocity (NCV) of motor nerves was obtained to divide the distance between two stimulation locations by the time it spends for electrical stimuli conducting between electrodes. The data recorded or calculated on the contralateral uninjured side was used for normalization.

4.9. FluoroGold (FG) retrograde tracing

To further confirm the reconstruction of neural connections, the sciatic nerve on the injured side was re-exposed and 5 μl of 5 % FG solution (Fluorochrome Inc., Denver, CO, USA) was injected into the regenerated nerve trunk 5 mm from the distal stump followed by the closure of the incision. One-week post-surgery, rats (n = 3 in each group) were transcardially perfused consecutively with saline and 4 % (v/v) paraformaldehyde in 0.1 M phosphate buffer. Spinal cord segments at L4, L5, L6, along with the corresponding DRGs were obtained and cut into 30-μm-thick of (for spinal cord) and 20-μm-thick (for DRGs) longitudinal sections on a cryostat. This was followed by photography under a confocal laser scanning microscope (TCS SP2; Leica, Wetzlar, Germany). The number of FG-labeled spinal cord motoneurons was directly counted and the percentage of FG-labeled DRG sensory neurons was calculated via dividing the FG-positive cell number by the total neuron number.

4.10. Histological evaluation and morphometric investigation of regenerated nerves and target muscles

Transverse sections of the regenerated nerve in the distal stump were subjected to Meyer's modified trichrome staining, immunofluorescence staining, and transmission electron microscopy (TEM), respectively. The photography of Meyer's modified trichrome staining carried out under light microscopy (Axio Imager 2, Zeiss, Oberkochen, Germany). To clearly show the regenerated axons and myelin, mouse anti-NF200 monoclonal antibody and rabbit anti-S100β polyclonal antibody (Sigma-Aldrich, USA) were applied to nerve sections and allowed to incubate overnight at 4 °C. The labelling was finished with a secondary antibody (Donkey anti-Mouse IgG-Alex-488, and Donkey anti-Rabbit IgG-Cy3) at 4 °C for 2 h. The photography was carried out under a confocal laser scanning microscope (TCS SP2, Leica, Wetzlar, Germany).

Besides, the gastrocnemius and anterior tibial muscles on the injured side and contralateral uninjured side were collected and weighed to calculate the wet weight ratio (the wet weight of muscle on the injured side is divided by that on the uninjured side), respectively. Followed by trimming and fixing in 4 % paraformaldehyde, the mid-belly of the gastrocnemius muscles was cut into transverse sections that underwent Masson's trichrome staining and photography by light microscopy. The longitudinal sections were subjected to double-staining with α-bungarotoxin and mouse anti-NF200 monoclonal antibody followed by photography under a confocal laser scanning microscope.

For TEM, nerve specimens were fixed in pre-cooled 2.5 % glutaraldehyde for 3 h, post-fixed with 1 % osmium tetraoxide solution for 1 h, washed, dehydrated, embedded in Epon 812 epoxy resin, and cut into ultra-thin sections of 60 nm thickness for staining with lead citrate and uranyl acetate. The stained sections were observed under a transmission electron microscope (JEOL Ltd., Tokyo, Japan), and images were taken from 20 random fields of each section. The number of myelin sheath layers, the thickness of myelin sheaths and the diameter of myelinated nerve fibers were quantified using Q550 IW image analysis system (Leica Imaging Systems Ltd., Cambridge, England) and the Leica QWin software package.

4.11. Sample preparation and microarray

Graft segments with both nerve stumps (0.2 cm) and nerve segments in the shame group were collected at 0.5 h, 1.5 h, 3 h, 6 h, 12 h, 1 d, 4 d, 7 d, 1 w, 2 w, 3 w, 4 w, 8 w, and 12 w post-surgery. The L4-6 DRGs were also harvested from animals across all groups after they were killed by cervical dislocation at the corresponding time points (0.5 h, 1.5 h, 3 h, 6 h, 12 h, 1 d, 4 d, 7 d, 1 w, 2 w, 3 w, 4 w). Total RNA was then extracted using Trizol (Life technologies, Carlsbad, CA) according to the manufacturer's instructions. RNA quality of each sample was determined using the Agilent Bioanalyzer 2100 (Agilent technologies, Santa Clara, CA) and Nanodrop ND1000 spectrophotometer (NanoDrop Technologies, Wilmington, DE). Microarray analysis was performed by an Agilent Microarray Scanner (Agilent Technologies) and the subsequent data compiled with Agilent feature extraction software. All steps from RNA amplification to the final scanner output were conducted by OE Biotechnology Company in Shanghai (China), and three biological replicates were performed for each time point. Total RNA was extracted from (input the type of your samples) using (input the kit used for RNA extraction) according to the manufacturer's specifications. RNA yield was determined using a NanoDrop 2000 spectrophotometer (Thermo Scientific, USA), and the integrity was evaluated using agarose gel electrophoresis stained with ethidium bromide. Gene microarrays from Agilent SurePrint G3 Rat Gene Expression 8 × 60K (~30,003) were applied in this work. Sample labeling and array hybridization were performed according to the Agilent One-Color Microarray-Based Gene Expression Analysis protocol (Agilent Technology). Briefly, total RNA from each sample was linearly amplified and labeled with Cy3-UTP. The labeled cRNAs were purified using the RNeasy Mini Kit (Qiagen). The concentration and specific activity of the labeled cRNAs (pmol Cy3/μg cRNA) were measured by NanoDrop ND-1000. 1 μg of each labeled cRNA was fragmented by adding 11 μl of 10X Blocking Agent and 2.2 μl of 25X Fragmentation Buffer, heating the mixture at 60 °C for 30 min, and finally adding 55 μl 2X GE Hybridization buffer to dilute the labeled cRNA. 100 μl of hybridization solution was dispensed into the gasket slide and fixed to the gene expression microarray slide. The slides were incubated for 17 h at 65 °C in an Agilent Hybridization Oven. The hybridized arrays were washed, fixed and scanned using the Agilent DNA Microarray Scanner.

4.12. Bioinformatics analysis

Agilent Feature Extraction software (version 12.0.1.1) was used to analyze acquired array images. Quantile normalization and subsequent data processing were performed with using the GeneSpring GX v12.0 software package (Agilent Technologies). After quantile normalization of the raw data, genes that were flagged in the Detected ("All Targets Value") category in at least 15 out of 60 samples were chosen for further

analysis. Differentially expressed genes with statistical significance were identified through Volcano Plot filtering. Hierarchical Clustering was performed using the Agilent GeneSpring GX software (version 12.0). GO and Pathway analysis were performed in the standard enrichment computation method.

Bioinformatics analysis was performed according to the protocols described previously [64]. Briefly, Euclidean distance calculation, PCA, and hierarchical clustering were performed based on log2-transformed mean-centered datasets as described previously [65]. A Euclidean distance heat map was created with the Heat Map Image Gene Pattern module. PCA was performed using the 'Population PCA' tool (http://cbdm.hms.harvard.edu/LabMembersPges/SD.html). Hierarchical clustering was performed with the Hierarchical Clustering module (based on Euclidean distance) from Gene Pattern and was visualized with the interactive tree of life (iTOL) v3 [66]. Analysis of GO categorical enrichment was performed with DAVID tools [67] while average expression profiles were calculated as described previously [11]. The Venn diagrams were created using the Venny 2.1.0 online tool [68]. The heat map of relative gene expression was generated using a GENE-E provided on the Broad Institute website (https://software.broadinstitute.org/GENE-E/index.html).

The core analysis tool within the Ingenuity Pathway Analysis suite (IPA, Ingenuity Systems, Redwood City, CA) was used to identify canonical pathways that are significantly overrepresented. To rank significance of pathways, the member genes of each pathway were extracted from IPA. Gene expression levels for samples in each group were retrieved and the expression of all genes was compared between 2 (of the 4) randomly selected groups using multivariate analysis of variance (see supplemental experimental procedures for more details). Transcriptional regulators and other genes associated with neurite/axon growth were compared to identify the regulators that are required for neurite/axon growth [43]. The interconnections and interactions among these genes were further examined to better understand the regulatory networks and model signaling pathways. A network is a graphical representation of the molecular relationships between molecules. Molecules are represented as nodes, and the biological relationship between two nodes is represented as an edge. All edges are supported by at least 1 reference from existing sources including scientific literature, textbooks, or canonical information stored in the Ingenuity® Knowledge Base. To create connections between molecules, the Build - Connect tool of IPA was used, with direct (solid line) and indirect (dotted line) relationships shown.

4.13. Real-time quantitative RT-PCR

Quantification was performed with a two-step reaction process: reverse transcription (RT) and PCR. Each RT reaction consisted of 0.5 μg RNA, 2 μl of PrimerScript Buffer, 0.5 μl of oligo dT, 0.5 μl of random hexamers and 0.5 μl of PrimerScript RT Enzyme Mix I (TaKaRa, Japan) for a total volume of 10 μl. Reactions were performed in a GeneAmp® PCR System 9700 (Applied Biosystems, USA) for 15 min at 37 °C, followed by heat inactivation of the reverse transcriptase for 5 s at 85 °C. The 10 μl RT reaction mix was then diluted 10 × in nuclease-free water and stored at −20 °C.

Real-time PCR was performed using LightCycler® 480 Real-time PCR Instrument (Roche, Swiss) with 10 μl PCR reaction mixture that included 1 μl of cDNA, 5 μl of 2X LightCycler® 480 SYBR Green I Master (Roche, Swiss), 0.2 μl of forward primer, 0.2 μl of reverse primer and 3.6 μl of nuclease-free water. Reactions were incubated in a 384-well optical plate (Roche, Swiss) at 95 °C for 10 min, followed by 40 cycles of 95 °C for 10 s, 60 °C for 30 s. Each sample was run in triplicate for analysis. At the end of the PCR cycles, melting curve analysis was performed to validate the specific generation of the expected PCR product. The expression levels of mRNAs were normalized to GAPDH and were calculated using the $2^{-\Delta\Delta Ct}$ method.

4.14. Western blot analysis

Protein samples were extracted from graft tissues. Equal masses of protein samples were separated by SDS-PAGE, and transferred to PVDF membranes that were blocked and reacted with primary antibodies according to the manufacturer's recommendations. The antibodies used include: CDKN2A (1:600, Abcam), TNFAIP6 (1:800, Abcam), ESR2 (1:400, Abcam), UCN (1:400, LifeSpan BioSciences), IL1B (1:1000, Abcam), VIP (1:1000, Abcam), NFKBIA (1:1000, Abcam), GAL (1:600, Santa), CSF1 (1:400, Santa), JUN (1:1000, Abcam), ARG1 (1:800, Abcam), FGF2 (1:1000, Abcam), ATF3 (1:1000, Abcam), ZFP36 (1:400, Millipore), CCL2 (1:1000, Millipore), GFI1 (1:400, Abcam), CCK (1:1000, Santa), RUNX2 (1:600, Abcam), TNFα (1:600, Abcam), and β-actin (1:4,000, Proteintech). The specific binding of primary antibody was detected by HRP-conjugated species-specific secondary antibody (Beyotime, Shanghai, China) and enhanced chemiluminescence (ECL) assay.

4.15. Immunohistochemistry

Immunohistochemical analysis was performed as described in a previous study [20]. Briefly, the TA muscle was dissected, post-fixed, dehydrated, and sectioned (8-μm-thick sections) using a cryostat. The sections were thaw-mounted onto poly-L-lysine-coated slides and stored at −20 °C prior to immunostaining. The slides were washed in phosphate-buffered saline (PBS) for 10 min at room temperature, blocked, and then incubated overnight at 4 °C with primary antibodies. After washing with PBS, the slides were incubated at 4 °C for 24 h with two secondary goat antibodies labeled with fluorescein (FITC): anti-mouse IgG-FITC (1:800; Abcam, Cambridge, MA, USA) and anti-rabbit IgG-cy3 (1:1000; Abcam, Cambridge, MA, USA). The slides were washed 3 times in PBS, covered with cover slip and visualized under a DMR fluorescent microscope (Leica Microsystems, Wetzlar, Germany).

4.16. Primary adult DRG neuron culture, infection and axon regrowth analysis

The L4-L6 DRGs were removed from the adult SD rats, and transferred to Ca^{2+}/Mg^{2+}-free Hibernate A (BrainBits, Springfield, IL), where the axon roots and dural tissue were manually removed. The DRGs were then transferred to 0.1 % collagenase type I (Sigma, St Louis, MO). Following 1.5 h incubation at 37 °C, the DRGs were dissociated in 0.25 % trypsin (Gibco) for an additional 15 min at 37 °C, and mechanically triturated through a pipette into the single cell suspension. To remove SCs, a partial purification step was performed by centrifugation at 900 rpm for 5 min on 15 % BSA in PBS solution (Sigma). The obtained DRG neurons were cultured on the coated plates in Neurobasal-A and B-27 minus insulin (Gibco) supplemented with penicillin–streptomycin (both 50 U/ml, Gibco). Primary cultured DRG neurons were infected with RNAi lentivirus targeting Ankrd1, Sbno2, Cdkn2a, Crem, Hoxb8, Zfp488, Zfp36, Gfi1, Esr2, Nfkbia, Csrnp1, or negative control (Genepharma, Shanghai, China), respectively, according to the manufacturer's instructions. Neurons were re-suspended and re-plated to allow neurites to regrow. After 20 h culture, DRG neurons were fixed with 4 % paraformaldehyde to undergo immunocytochemistry with anti-β-Tubulin III antibody (Sigma) to observe axon outgrowth. Images were acquired by microscopy (Zeiss, Axio Imager M2m, Carl Zeiss, Oberkochen, Germany). We quantified the maximum length of neurites (longer than its soma diameter) of each neuron using Neuron J software in ImageJ. For cell axons counting, over 100 cells were counted in each group ($n > 100$).

4.17. Statistical analysis

All samples were analyzed in at least triplicate. Data are presented as

means ± SEM. Multiple comparisons were performed with one-way ANOVA plus Dunnett's multiple comparisons post hoc *t*-test. Statistical analysis was carried out using SPSS Statistics 22.0 software package (IBM, Chicago, Illinois).

Funding

This work was graciously supported by National Natural Science Foundation of China (Grant No. 31730031, 82172104, 81873767), National Key Research and Development Program of China (2017YFA0104703), Jiangsu Provincial Key Medical Center, Jiangsu Provincial Medical Innovation Center (CXZX202212), Jiangsu Provincial Medical Key Discipline (ZDXK202240), the Priority Academic Program Development of Jiangsu Higher Education Institutions (PAPD), and Technology Project of Nantong (MS22022008).

Availability of data and materials

All the data supporting the findings of this study are available within the paper and the raw and analyzed datasets generated during the study are available for research purposes from the corresponding authors on reasonable request.

Author disclosure statement

No competing financial interests exist.

Ethics approval and consent to participate

Adult female Sprague-Dawley (SD) rats were acquired from the Experimental Animal Center of Nantong University (License No. SYXK (Su) 2017-0046). All studies complied with all relevant animal use guidelines and ethical regulations. All animal use and study protocols were approved by the Administration Committee of Experimental Animals, Jiangsu Province, China, in accordance with the guidelines of the Institutional Animal Care and Use Committee, Nantong University, China (Inspection No: 20190225-004).

Consent for publication

Not applicable.

CRediT authorship contribution statement

Chengbin Xue: Conceptualization, Data curation, Formal analysis, Funding acquisition, Investigation, Methodology, Project administration, Resources, Software, Validation, Visualization, Writing – original draft, Writing – review & editing. **Hui Zhu:** Data curation, Formal analysis, Funding acquisition, Investigation, Project administration, Validation, Writing – original draft, Writing – review & editing. **Hongkui Wang:** Data curation, Formal analysis, Investigation, Methodology, Project administration, Resources, Validation, Visualization. **Yaxian Wang:** Conceptualization, Data curation, Formal analysis, Investigation, Methodology, Project administration, Resources, Software, Validation. **Xi Xu:** Data curation, Formal analysis, Investigation, Methodology, Project administration, Resources, Visualization. **Songlin Zhou:** Investigation, Methodology, Resources, Software, Validation, Visualization. **Dong Liu:** Conceptualization, Resources, Visualization. **Yahong Zhao:** Methodology, Project administration, Resources, Visualization. **Tianmei Qian:** Data curation, Investigation, Methodology, Project administration. **Qi Guo:** Data curation, Investigation, Methodology, Project administration, Resources. **Jin He:** Data curation, Software, Validation, Visualization. **Kairong Zhang:** Data curation, Formal analysis, Software, Validation, Visualization. **Yun Gu:** Formal analysis, Investigation, Resources, Software. **Leilei Gong:** Data curation, Formal analysis, Investigation. **Jian Yang:** Data curation, Formal analysis, Investigation. **Sheng Yi:** Data curation, Formal analysis, Software, Visualization. **Bin Yu:** Formal analysis, Investigation, Resources. **Yongjun Wang:** Investigation, Supervision, Visualization. **Yan Liu:** Investigation, Resources, Supervision. **Yumin Yang:** Investigation, Project administration, Resources. **Fei Ding:** Resources, Supervision. **Xiaosong Gu:** Conceptualization, Supervision, Writing – original draft, Writing – review & editing.

Declaration of competing interest

C.B.X., F.D., Y.G., Y.M.Y., Y.J.W., L.L.G., and X.S.G. are inventors on the Chinese patent (ZL201310028903.6), PCT (WO2014114043A1), Eurasian Patent, (EA201591373A1), US patent (US9492589 B2), Australian Patent (2013375655), European Patent (EP2949349B1.), and Brazilian patent (BR112015017174A2) that covers the fabrication of tissue engineered nerve *in vitro* via skin-derived precursor-induced Schwann cell-mediated chitosan/silk fibroin-fabricated tissue-engineered nerve graft.

Acknowledgements

We would like to thank professor Jie Liu from Nantong University, Han-Jun Kim and Peyton Tebon from University of California, Los Angeles for their help in English editing.

Appendix A. Supplementary data

Supplementary data to this article can be found online at https://doi.org/10.1016/j.bioactmat.2023.11.016.

References

[1] X. Tang, H. Qin, X. Gu, X. Fu, China's landscape in regenerative medicine, Biomaterials 124 (2017) 78–94.
[2] X. Gu, F. Ding, D.F. Williams, Neural tissue engineering options for peripheral nerve regeneration, Biomaterials 35 (24) (2014) 6143–6156.
[3] X. Gu, Biodegradable materials and the tissue engineering of nerves, Engineering 7 (12) (2021) 1700–1703.
[4] X. Gu, Recent Progress in Biomaterials-Tissue Engineering, 2022. Engineering.
[5] M. Hvistendahl, China's push in tissue engineering, Science 338 (6109) (2012) 900–902.
[6] S. Kehoe, X.F. Zhang, D. Boyd, FDA approved guidance conduits and wraps for peripheral nerve injury: a review of materials and efficacy, Injury 43 (5) (2012) 553–572.
[7] Y.S. Kim, M.M. Smoak, A.J. Melchiorri, A.G. Mikos, An Overview of the tissue engineering market in the United States from 2011 to 2018, Tissue Eng. 25 (1–2) (2019) 1–8.
[8] K.D. Gribble, L.J. Walker, L. Saint-Amant, J.Y. Kuwada, M. Granato, The synaptic receptor Lrp4 promotes peripheral nerve regeneration, Nat. Commun. 9 (1) (2018) 2389.
[9] A.-L. Cattin, A.C. Lloyd, The multicellular complexity of peripheral nerve regeneration, Curr. Opin. Neurobiol. 39 (2016) 38–46.
[10] Y.-L. Weng, X. Wang, R. An, J. Cassin, C. Vissers, Y. Liu, Y. Liu, T. Xu, X. Wang, S.Z. H. Wong, J. Joseph, L.C. Dore, Q. Dong, W. Zheng, P. Jin, H. Wu, B. Shen, X. Zhuang, C. He, K. Liu, H. Song, G.-l. Ming, Epitranscriptomic m6A regulation of axon regeneration in the adult mammalian nervous system, Neuron 97 (2) (2018) 313–325, e6.
[11] Q. Guo, H. Zhu, H. Wang, P. Zhang, S. Wang, Z. Sun, S. Li, C. Xue, X. Gu, S. Cui, Transcriptomic landscapes of immune response and axonal regeneration by integrative analysis of molecular pathways and interactive networks post-sciatic nerve transection, Front. Neurosci. 12 (2018) 457.
[12] B. Yu, T. Qian, Y. Wang, S. Zhou, G. Ding, F. Ding, X. Gu, miR-182 inhibits Schwann cell proliferation and migration by targeting FGF9 and NTM, respectively at an early stage following sciatic nerve injury, Nucleic Acids Res. 40 (20) (2012) 10356–10365.
[13] Z. Zhang, B. Yu, Y. Gu, S. Zhou, T. Qian, Y. Wang, G. Ding, F. Ding, X. Gu, Fibroblast-derived tenascin-C promotes Schwann cell migration through β1-integrin dependent pathway during peripheral nerve regeneration, Glia 64 (3) (2015) 374–385.
[14] K.J.L. Fernandes, I.A. McKenzie, P. Mill, K.M. Smith, M. Akhavan, F. Barnabé-Heider, J. Biernaskie, A. Junek, N.R. Kobayashi, J.G. Toma, D.R. Kaplan, P. A. Labosky, V. Rafuse, C.-C. Hui, F.D. Miller, A dermal niche for multipotent adult skin-derived precursor cells, Nat. Cell Biol. 6 (11) (2004) 1082–1093.
[15] J. Biernaskie, M. Paris, O. Morozova, B.M. Fagan, M. Marra, L. Pevny, F.D. Miller, SKPs derive from hair follicle precursors and exhibit properties of adult dermal stem cells, Cell Stem Cell 5 (6) (2009) 610–623.

[16] J.G. Toma, M. Akhavan, K.J.L. Fernandes, F. Barnabé-Heider, A. Sadikot, D. R. Kaplan, F.D. Miller, Isolation of multipotent adult stem cells from the dermis of mammalian skin, Nat. Cell Biol. 3 (9) (2001) 778–784.
[17] I.A. McKenzie, J. Biernaskie, J.G. Toma, R. Midha, F.D. Miller, Skin-derived precursors generate myelinating Schwann cells for the injured and dysmyelinated nervous system, J. Neurosci. 26 (24) (2006) 6651–6660.
[18] S. Walsh, J. Biernaskie, S.W.P. Kemp, R. Midha, Supplementation of acellular nerve grafts with skin derived precursor cells promotes peripheral nerve regeneration, Neuroscience 164 (3) (2009) 1097–1107.
[19] S.K. Walsh, T. Gordon, B.M.J. Addas, S.W.P. Kemp, R. Midha, Skin-derived precursor cells enhance peripheral nerve regeneration following chronic denervation, Exp. Neurol. 223 (1) (2010) 221–228.
[20] Y. Gu, J. Zhu, C. Xue, Z. Li, F. Ding, Y. Yang, X. Gu, Chitosan/silk fibroin-based, Schwann cell-derived extracellular matrix-modified scaffolds for bridging rat sciatic nerve gaps, Biomaterials 35 (7) (2014) 2253–2263.
[21] C. Xue, H. Ren, H. Zhu, X. Gu, Q. Guo, Y. Zhou, J. Huang, S. Wang, G. Zha, J. Gu, Y. Yang, Y. Gu, X. Gu, Bone marrow mesenchymal stem cell-derived acellular matrix-coated chitosan/silk scaffolds for neural tissue regeneration, J. Mater. Chem. B 5 (6) (2017) 1246–1257.
[22] J.A. Biernaskie, I.A. McKenzie, J.G. Toma, F.D. Miller, Isolation of skin-derived precursors (SKPs) and differentiation and enrichment of their Schwann cell progeny, Nat. Protoc. 1 (6) (2007) 2803–2812.
[23] M. Stephenson, W. Grayson, Recent Advances in Bioreactors for Cell-Based Therapies, F1000Research, 2018, p. 7.
[24] J. Bartolucci, F.J. Verdugo, P.L. González, R.E. Larrea, E. Abarzua, C. Goset, P. Rojo, I. Palma, R. Lamich, P.A. Pedreros, G. Valdivia, V.M. Lopez, C. Nazzal, F. Alcayaga-Miranda, J. Cuenca, M.J. Brobeck, A.N. Patel, F.E. Figueroa, M. Khoury, Safety and efficacy of the intravenous infusion of umbilical cord mesenchymal stem cells in patients with heart failure, Circ. Res. 121 (10) (2017) 1192–1204.
[25] C. Xue, H. Zhu, D. Tan, H. Ren, X. Gu, Y. Zhao, P. Zhang, Z. Sun, Y. Yang, J. Gu, Y. Gu, X. Gu, Electrospun silk fibroin-based neural scaffold for bridging a long sciatic nerve gap in dogs, J. Tissue Eng. Regener. Med. 12 (2) (2017) e1143–e1153.
[26] B.S. Spearman, V.H. Desai, S. Mobini, M.D. McDermott, J.B. Graham, K.J. Otto, J. W. Judy, C.E. Schmidt, Tissue-engineered peripheral nerve interfaces, Adv. Funct. Mater. 28 (12) (2017), 1701713.
[27] B.-C. Jeong, J.H. Kim, K. Kim, I. Kim, S. Seong, N. Kim, ATF3 modulates calcium signaling in osteoclast differentiation and activity by associating with c-Fos and NFATc1 proteins, Bone 95 (2017) 33–40.
[28] L. Min, Y. Ji, L. Bakiri, Z. Qiu, J. Cen, X. Chen, L. Chen, H. Scheuch, H. Zheng, L. Qin, K. Zatloukal, L. Hui, E.F. Wagner, Liver cancer initiation is controlled by AP-1 through SIRT6-dependent inhibition of survivin, Nat. Cell Biol. 14 (11) (2012) 1203–1211.
[29] L. Bakiri, R. Hamacher, O. Graña, A. Guío-Carrión, R. Campos-Olivas, L. Martinez, H.P. Dienes, M.K. Thomsen, S.C. Hasenfuss, E.F. Wagner, Liver carcinogenesis by FOS-dependent inflammation and cholesterol dysregulation, J. Exp. Med. 214 (5) (2017) 1387–1409.
[30] T. Vierbuchen, E. Ling, C.J. Cowley, C.H. Couch, X. Wang, D.A. Harmin, C.W. M. Roberts, M.E. Greenberg, AP-1 transcription factors and the BAF complex mediate signal-dependent enhancer selection, Mol. Cell 68 (6) (2017) 1067–1082, e12.
[31] S. Quintes, B.G. Brinkmann, M. Ebert, F. Fröb, T. Kungl, F.A. Arlt, V. Tarabykin, D. Huylebroeck, D. Meijer, U. Suter, M. Wegner, M.W. Sereda, K.-A. Nave, Zeb2 is essential for Schwann cell differentiation, myelination and nerve repair, Nat. Neurosci. 19 (8) (2016) 1050–1059.
[32] A.I. Nascimento, F.M. Mar, M.M. Sousa, The intriguing nature of dorsal root ganglion neurons: linking structure with polarity and function, Prog. Neurobiol. 168 (2018) 86–103.
[33] Y. Cho, Jung E. Shin, Eric E. Ewan, Young M. Oh, W. Pita-Thomas, V. Cavalli, Activating injury-responsive genes with hypoxia enhances axon regeneration through neuronal HIF-1α, Neuron 88 (4) (2015) 720–734.
[34] D. Kalladka, J. Sinden, K. Pollock, C. Haig, J. McLean, W. Smith, A. McConnachie, C. Santosh, P.M. Bath, L. Dunn, K.W. Muir, Human neural stem cells in patients with chronic ischaemic stroke (PISCES): a phase 1, first-in-man study, Lancet 388 (10046) (2016) 787–796.
[35] J. Panés, D. García-Olmo, G. Van Assche, J.F. Colombel, W. Reinisch, D. C. Baumgart, A. Dignass, M. Nachury, M. Ferrante, L. Kazemi-Shirazi, J. C. Grimaud, F. de la Portilla, E. Goldin, M.P. Richard, A. Leselbaum, S. Danese, Expanded allogeneic adipose-derived mesenchymal stem cells (Cx601) for complex perianal fistulas in Crohn's disease: a phase 3 randomised, double-blind controlled trial, Lancet 388 (10051) (2016) 1281–1290.
[36] John E. Wagner, Claudio G. Brunstein, Anthony E. Boitano, Todd E. DeFor, D. McKenna, D. Sumstad, Bruce R. Blazar, J. Tolar, C. Le, J. Jones, Michael P. Cooke, Conrad C. Bleul, Phase I/II trial of StemRegenin-1 expanded umbilical cord blood hematopoietic stem cells supports testing as a stand-alone graft, Cell Stem Cell 18 (1) (2016) 144–155.
[37] Z. Chen, S. Pradhan, C. Liu, L.Q. Le, Skin-derived precursors as a source of progenitors for cutaneous nerve regeneration, Stem Cell. 30 (10) (2012) 2261–2270.
[38] M.P. Clements, E. Byrne, L.F. Camarillo Guerrero, A.-L. Cattin, L. Zakka, A. Ashraf, J.J. Burden, S. Khadayate, A.C. Lloyd, S. Marguerat, S. Parrinello, The wound microenvironment reprograms Schwann cells to invasive mesenchymal-like cells to drive peripheral nerve regeneration, Neuron 96 (1) (2017) 98–114, e7.
[39] Y.-L. Weng, R. An, J. Cassin, J. Joseph, R. Mi, C. Wang, C. Zhong, S.-G. Jin, G. P. Pfeifer, A. Bellacosa, X. Dong, A. Hoke, Z. He, H. Song, G.-l. Ming, An intrinsic epigenetic barrier for functional axon regeneration, Neuron 94 (2) (2017) 337–346, e6.
[40] M.A. Anderson, T.M. O'Shea, J.E. Burda, Y. Ao, S.L. Barlatey, A.M. Bernstein, J. H. Kim, N.D. James, A. Rogers, B. Kato, A.L. Wollenberg, R. Kawaguchi, G. Coppola, C. Wang, T.J. Deming, Z. He, G. Courtine, M.V. Sofroniew, Required growth facilitators propel axon regeneration across complete spinal cord injury, Nature 561 (7723) (2018) 396–400.
[41] G. Poplawski, T. Ishikawa, C. Brifault, C. Lee-Kubli, R. Regestam, K.W. Henry, Y. Shiga, H. Kwon, S. Ohtori, S.L. Gonias, W.M. Campana, Schwann cells regulate sensory neuron gene expression before and after peripheral nerve injury, Glia 66 (8) (2018) 1577–1590.
[42] Michio W. Painter, A. Brosius Lutz, Y.-C. Cheng, A. Latremoliere, K. Duong, Christine M. Miller, S. Posada, Enrique J. Cobos, Alice X. Zhang, Amy J. Wagers, Leif A. Havton, B. Barres, T. Omura, Clifford J. Woolf, Diminished Schwann cell repair responses underlie age-associated impaired axonal regeneration, Neuron 83 (2) (2014) 331–343.
[43] M. Mahar, V. Cavalli, Intrinsic mechanisms of neuronal axon regeneration, Nat. Rev. Neurosci. 19 (6) (2018) 323–337.
[44] V. Chandran, G. Coppola, H. Nawabi, T. Omura, R. Versano, Eric A. Huebner, A. Zhang, M. Costigan, A. Yekkirala, L. Barrett, A. Blesch, I. Michaelevski, J. Davis-Turak, F. Gao, P. Langfelder, S. Horvath, Z. He, L. Benowitz, M. Fainzilber, M. Tuszynski, Clifford J. Woolf, Daniel H. Geschwind, A systems-level analysis of the peripheral nerve intrinsic axonal growth program, Neuron 89 (5) (2016) 956–970.
[45] C. Yoon, Roman J. Giger, Inside out: core network of transcription factors drives axon regeneration, Neuron 89 (5) (2016) 881–884.
[46] R. Reuten, T.R. Patel, M. McDougall, N. Rama, D. Nikodemus, B. Gibert, J.-G. Delcros, C. Prein, M. Meier, S. Metzger, Z. Zhou, J. Kaltenberg, K.K. McKee, T. Bald, T. Tüting, P. Zigrino, V. Djonov, W. Bloch, H. Clausen-Schaumann, E. Poschl, P.D. Yurchenco, M. Ehrbar, P. Mehlen, J. Stetefeld, M. Koch, Structural decoding of netrin-4 reveals a regulatory function towards mature basement membranes, Nat. Commun. 7 (1) (2016), 13515.
[47] A.-L. Cattin, Jemima J. Burden, L. Van Emmenis, Francesca E. Mackenzie, Julian J. A. Hoving, N. Garcia Calavia, Y. Guo, M. McLaughlin, Laura H. Rosenberg, V. Quereda, D. Jamecna, I. Napoli, S. Parrinello, T. Enver, C. Ruhrberg, Alison C. Lloyd, Macrophage-induced blood vessels guide Schwann cell-mediated regeneration of peripheral nerves, Cell 162 (5) (2015) 1127–1139.
[48] J. Rouwkema, A. Khademhosseini, Vascularization and angiogenesis in tissue engineering: beyond creating static networks, Trends Biotechnol. 34 (9) (2016) 733–745.
[49] J.E. Nichols, S. La Francesca, J.A. Niles, S.P. Vega, L.B. Argueta, L. Frank, D. C. Christiani, R.B. Pyles, B.E. Himes, R. Zhang, S. Li, J. Sakamoto, J. Rhudy, G. Hendricks, F. Begarani, X. Liu, I. Patrikeev, R. Pal, E. Usheva, G. Vargas, A. Miller, L. Woodson, A. Wacher, M. Grimaldo, D. Weaver, R. Mlcak, J. Cortiella, Production and transplantation of bioengineered lung into a large-animal model, Sci. Transl. Med. 10 (452) (2018).
[50] J. Fu, D.-A. Wang, In situ organ-specific vascularization in tissue engineering, Trends Biotechnol. 36 (8) (2018) 834–849.
[51] H. Bae, A.S. Puranik, R. Gauvin, F. Edalat, B. Carrillo-Conde, N.A. Peppas, A. Khademhosseini, Building vascular networks, Sci. Transl. Med. 4 (160) (2012) 160ps23.
[52] P. Carmeliet, M. Tessier-Lavigne, Common mechanisms of nerve and blood vessel wiring, Nature 436 (7048) (2005) 193–200.
[53] A. Eichmann, F.L. Noble, M. Autiero, P. Carmeliet, Guidance of vascular and neural network formation, Curr. Opin. Neurobiol. 15 (1) (2005) 108–115.
[54] B. Larrivée, C. Freitas, S. Suchting, I. Brunet, A. Eichmann, Guidance of vascular development, Circ. Res. 104 (4) (2009) 428–441.
[55] P. Carmeliet, Blood vessels and nerves: common signals, pathways and diseases, Nat. Rev. Genet. 4 (9) (2003) 710–720.
[56] B.M. Weinstein, Vessels and nerves: marching to the same tune, Cell 120 (3) (2005) 299–302.
[57] R.H. Adams, K. Alitalo, Molecular regulation of angiogenesis and lymphangiogenesis, Nat. Rev. Mol. Cell Biol. 8 (6) (2007) 464–478.
[58] S. Zacchigna, C. Ruiz de Almodovar, P. Carmeliet, Similarities between angiogenesis and neural development: what small animal models can tell us, Curr. Top. Dev. Biol. 80 (2008) 1–55.
[59] B. Zhao, C. Chun, Z. Liu, M.A. Horswill, K. Pramanik, G.A. Wilkinson, R. Ramchandran, R.Q. Miao, Nogo-B receptor is essential for angiogenesis in zebrafish via Akt pathway, Blood 116 (24) (2010) 5423–5433.
[60] S. Sawamiphak, S. Seidel, C.L. Essmann, G.A. Wilkinson, M.E. Pitulescu, T. Acker, A. Acker-Palmer, Ephrin-B2 regulates VEGFR2 function in developmental and tumour angiogenesis, Nature 465 (7297) (2010) 487–491.
[61] F.J. Stam, H.D. MacGillavry, N.J. Armstrong, M.C.M. De Gunst, Y. Zhang, R.E. Van Kesteren, A.B. Smit, J. Verhaagen, Identification of candidate transcriptional modulators involved in successful regeneration after nerve injury, Eur. J. Neurosci. 25 (12) (2007) 3629–3637.
[62] S. Päiväläinen, M. Nissinen, H. Honkanen, O. Lahti, S.M. Kangas, J. Peltonen, S. Peltonen, A.M. Heape, Myelination in mouse dorsal root ganglion/Schwann cell cocultures, Mol. Cell. Neurosci. 37 (3) (2008) 568–578.
[63] M. Yao, Y. Zhou, C. Xue, H. Ren, S. Wang, H. Zhu, X. Gu, X. Gu, J. Gu, Repair of rat sciatic nerve defects by using allogeneic bone marrow mononuclear cells combined with chitosan/silk fibroin scaffold, Cell Transplant. 25 (5) (2016) 983–993.
[64] S. Li, C. Xue, Y. Yuan, R. Zhang, Y. Wang, Y. Wang, B. Yu, J. Liu, F. Ding, Y. Yang, X. Gu, The transcriptional landscape of dorsal root ganglia after sciatic nerve transection, Sci. Rep. 5 (1) (2015), 16888.

[65] M. Mingueneau, T. Kreslavsky, D. Gray, T. Heng, R. Cruse, J. Ericson, S. Bendall, M. H. Spitzer, G.P. Nolan, K. Kobayashi, H. von Boehmer, D. Mathis, C. Benoist, The transcriptional landscape of αβ T cell differentiation, Nat. Immunol. 14 (6) (2013) 619–632.

[66] I. Letunic, P. Bork, Interactive tree of life (iTOL) v3: an online tool for the display and annotation of phylogenetic and other trees, Nucleic Acids Res. 44 (W1) (2016) W242–W245.

[67] S.-H. Yu, K.-Y. Zhu, J. Chen, X.-Z. Liu, P.-F. Xu, W. Zhang, L. Yan, H.-Z. Guo, J. Zhu, JMJD3 facilitates C/EBPβ-centered transcriptional program to exert oncorepressor activity in AML, Nat. Commun. 9 (1) (2018) 3369.

[68] C. Cencioni, F. Spallotta, M. Savoia, C. Kuenne, S. Guenther, A. Re, S. Wingert, M. Rehage, D. Sürün, M. Siragusa, J.G. Smith, F. Schnütgen, H. von Melchner, M. A. Rieger, F. Martelli, A. Riccio, I. Fleming, T. Braun, A.M. Zeiher, A. Farsetti, C. Gaetano, Zeb1-Hdac2-eNOS circuitry identifies early cardiovascular precursors in naive mouse embryonic stem cells, Nat. Commun. 9 (1) (2018) 1281.